

ORNL/TM-2017/718  
CRADA/NFE-16-06212

# Integrated Predictive Tools for Customizing Microstructure and Material Properties of Additively Manufactured Aerospace Components



Approved for Public Release

B. Radhakrishnan (ORNL)  
J-L. Fattebert (ORNL)  
S.B. Gorti (ORNL)  
T. Haxhimali (LLNL)  
T. El-Wardany (UTRC)  
R. Acharya (UTRC)  
A. Staroselsky (UTRC)

**OAK RIDGE NATIONAL LABORATORY**

MANAGED BY UT-BATTELLE FOR THE US DEPARTMENT OF ENERGY

**Date** Nov 13, 2017

## DOCUMENT AVAILABILITY

Reports produced after January 1, 1996, are generally available free via US Department of Energy (DOE) SciTech Connect.

**Website** <http://www.osti.gov/scitech/>

Reports produced before January 1, 1996, may be purchased by members of the public from the following source:

National Technical Information Service  
5285 Port Royal Road  
Springfield, VA 22161  
**Telephone** 703-605-6000 (1-800-553-6847)  
**TDD** 703-487-4639  
**Fax** 703-605-6900  
**E-mail** [info@ntis.gov](mailto:info@ntis.gov)  
**Website** <http://www.ntis.gov/help/ordermethods.aspx>

Reports are available to DOE employees, DOE contractors, Energy Technology Data Exchange representatives, and International Nuclear Information System representatives from the following source:

Office of Scientific and Technical Information  
PO Box 62  
Oak Ridge, TN 37831  
**Telephone** 865-576-8401  
**Fax** 865-576-5728  
**E-mail** [reports@osti.gov](mailto:reports@osti.gov)  
**Website** <http://www.osti.gov/contact.html>

This report was prepared as an account of work sponsored by an agency of the United States Government. Neither the United States Government nor any agency thereof, nor any of their employees, makes any warranty, express or implied, or assumes any legal liability or responsibility for the accuracy, completeness, or usefulness of any information, apparatus, product, or process disclosed, or represents that its use would not infringe privately owned rights. Reference herein to any specific commercial product, process, or service by trade name, trademark, manufacturer, or otherwise, does not necessarily constitute or imply its endorsement, recommendation, or favoring by the United States Government or any agency thereof. The views and opinions of authors expressed herein do not necessarily state or reflect those of the United States Government or any agency thereof.

High Performance Computing for Manufacturing (HPC4Mfg)

**INTEGRATED PREDICTIVE TOOLS FOR CUSTOMIZING MICROSTRUCTURE  
AND MATERIAL PROPERTIES OF ADDITIVELY MANUFACTURED  
AEROSPACE COMPONENTS**

B. Radhakrishnan (ORNL)  
J-L. Fattebert (ORNL)  
T. Haxhimali (LLNL)  
S.B. Gorti (ORNL)  
T. El-Wardany (UTRC)  
R. Acharya (UTRC)  
A. Staroselsky (UTRC)

Date Published: Nov 13, 2017

Prepared by  
OAK RIDGE NATIONAL LABORATORY  
Oak Ridge, Tennessee 37831-6283  
managed by  
UT-BATTELLE, LLC  
for the  
US DEPARTMENT OF ENERGY  
under contract DE-AC05-00OR22725

Approved for Public Release

## 1. ABSTRACT

Additive Manufacturing (AM) refers to a process by which digital three-dimensional (3-D) design data is converted to build up a component by depositing material layer-by-layer. United Technologies Corporation (UTC) is currently involved in fabrication and certification of several AM aerospace structural components made from aerospace materials. This is accomplished by using optimized process parameters determined through numerous design-of-experiments (DOE)-based studies. Certification of these components is broadly recognized as a significant challenge, with long lead times, very expensive new product development cycles and very high energy consumption. Because of these challenges, United Technologies Research Center (UTRC), together with UTC business units have been developing and validating an advanced physics-based process model. The specific goal is to develop a physics-based framework of an AM process and reliably predict fatigue properties of built-up structures as based on detailed solidification microstructures. Microstructures are predicted using process control parameters including energy source power, scan velocity, deposition pattern, and powder properties. The multi-scale multi-physics model requires solution and coupling of governing physics that will allow prediction of the thermal field and enable solution at the microstructural scale. The state-of-the-art approach to solve these problems requires a huge computational framework and this kind of resource is only available within academia and national laboratories.

The project utilized the parallel phase-fields codes at Oak Ridge National Laboratory (ORNL) and Lawrence Livermore National Laboratory (LLNL), along with the high-performance computing (HPC) capabilities existing at the two labs to demonstrate the simulation of multiple dendrite growth in three-dimensions (3-D). The LLNL code AMPE was used to implement the UTRC phase field model that was previously developed for a model binary alloy, and the simulation results were compared against the UTRC simulation results, followed by extension of the UTRC model to simulate multiple dendrite growth in 3-D. The ORNL MEUMAPPS code was used to simulate dendritic growth in a model ternary alloy with the same equilibrium solidification range as the Ni-base alloy 718 using realistic model parameters, including thermodynamic integration with a Calphad based model for the ternary alloy. Implementation of the UTRC model in AMPE met with several numerical and parametric issues that were resolved and good comparison between the simulation results obtained by the two codes was demonstrated for two dimensional (2-D) dendrites. 3-D dendrite growth was then demonstrated with the AMPE code using non-dimensional parameters obtained in 2-D simulations. Multiple dendrite growth in 2-D and 3-D were demonstrated using ORNL's MEUMAPPS code using simple thermal boundary conditions. MEUMAPPS was then modified to incorporate the complex, time-dependent thermal boundary conditions obtained by UTRC's thermal modeling of single track AM experiments to drive the phase field simulations. The results were in good agreement with UTRC's experimental measurements.

## 2. STATEMENT OF OBJECTIVES

The main objectives of the project are (1) to incorporate the phase field model developed by UTRC in the phase field simulation codes at ORNL and LLNL to demonstrate massively parallel simulations of multiple dendrites in three dimensions (3-D), (2) to extend the model to simulate dendritic solidification in the Ni-base alloy 718 by coupling with AM-process-specific thermal boundary conditions provided by UTRC and (3) to compare simulation predictions with experimental input from UTRC. In order to realize the above objectives, it was necessary to modify / enhance the existing phase field codes at ORNL and LLNL to adapt the codes to handle alloy and process parameters characteristic of the AM process. Specifically, the following project tasks describe the technical problems that were undertaken.

- Modify ORNL and LLNL phase-field codes to handle AM solidification problems by incorporating the features of UTRC model
- Simulate benchmark solidification problem using a model ternary alloy and compare ORNL and LLNL code performance with respect to scaling
- Demonstrate evolution of 3-D solidification microstructure during AM of alloy IN 718 using the selected phase-field code
- Validate predictions using UTRC experimental results on microsegregation, primary and dendrite arm spacing as a function of process parameters, and further refine model/code to improve predictions

### 3. DENEFITIS TO FUNDING DOE OFFICE MISSION

The proposed R&D is a unique opportunity to test the feasibility of utilizing the high performance computing facilities at the National Laboratories and their parallel computing codes to solve an important technical problem relating to additive manufacturing. The program allowed for enhancements to be performed on the national laboratory codes so that they could be directly applied to an industrial process and a structural alloy relevant to the aerospace industry. The experience gained from running such practical applications will make the codes more robust and will enable their reliable utilization in future industrial applications. The goal of this project is to support and accelerate innovative structural design, process qualification and certification for AM components and it is truly relevant to the goals of DOE's HPC4Mfg program.

### 4. TECHNICAL DISCUSSION OF WORK

#### 4.1 Introduction

Important facets of the AM technologies include design, materials, processes, and machines [1]. Computation of continuum based energy insertion [2-10], melt pool geometry [11-20], residual stress and distortion [11, 21-24], temperature distribution in the melt pool and transient history as well as defects prediction as function of process parameters are all well-established [25]. Microstructure models including the effect of secondary elements and rapid solidification were developed for solving directional solidification problem in casting and welding [26-36]. Considerations of detailed powder bed based numerical models are currently being developed to computationally model the melting of powder and resulting densification, thus resolving randomly distributed individual powder particles in 3D [37, 38]. On the other hand, physics- based models relating process parameters to microstructure, properties and performance are needed for new alloys including aerospace alloys to optimize mechanical properties, control fatigue properties and reduce surface roughness. UTRC AM modeling development to predict microstructure evolution and mechanical properties indicates that this part of the modeling activities requires tight coupling with the heat transfer model to obtain the initial melt pool geometry and transient temperature history as inputs for the microstructure evolution model. In addition, multi-component alloy thermodynamics and kinetics and potential non-equilibrium effects on solute partitioning between the solid and the liquid have to be integrated with the evolution equations for high fidelity prediction of mushy zone geometry and microstructure morphology governing dendritic or equiaxed features. Such modeling within the context of AM and HPC are only beginning to emerge. Since there are several alloying elements in aerospace superalloys, numerical simulation for each individual element is computationally expensive and requires significant effort to either: (1) reduce the computational complexity by using a reduced number of secondary elements, or; (2) solve multiple phase field algorithms considering the contribution of each element. The second approach is based on reduced spatial and temporal solution since modeling of the full domain is virtually impossible for a given numerical scheme. Hence the first approach with reduced number of elements is widely accepted and also developed

by UTRC by considering the contribution of one secondary element [39]. Approach proposed by UTRC is reliant on computational fluid dynamics (CFD) to obtain the inputs for mushy zone geometry and is capable of predicting several microstructural features including morphology, dendrite orientation, primary dendrite arm spacing (PDAS), secondary dendrite arm spacing (SDAS), concentration distribution and grain size [39]. The existing algorithm developed by UTRC is capable of computing the 2D microstructure efficiently.

## 4.2 Motivation

Both ORNL and LLNL are actively working on massively parallel phase field simulations using two different numerical approaches with their own inherent advantages in the solution of the evolution equations. The lessons learned from these simulations would be extremely valuable in choosing the right approach to efficiently solve the evolution equations developed by UTRC so that adequate validation and meaningful production runs with chosen process parameters can be completed within the project period. This is the critical first step in implementing the integrated UTRC framework for AM process optimization and new alloy development. AM of metallic components will be affordable, durable, and structurally efficient when the above-mentioned technical challenges will be realized and solutions to the specific problems are addressed through advanced physics based modeling. The goal of this project is to support and accelerate innovative structural design, process qualification and certification for AM components and it is truly relevant to the goals of HPC4Mfg program.

Consideration of 3D dendritic growth required that the current UTRC numerical scheme for a pseudo-binary alloy to run on 128 processors for one month just to simulate a few dendrites. For example, a simple problem of dendritic growth in microstructural scale of AM requires 768 GPUs each containing 768 CPUs to solve the problem for 100 microseconds during microstructure evolution [40]. Performing these simulations for the full-scale 3D geometry will allow solving for mutual growth competition among differently oriented dendrites and will reveal the effect of accurate temperature distribution on the dendrite growth. The handling of large output data is an important factor for the efficiency and usability of the code for large scale industrial solution. A large-scale parallel computation and HPC clusters are required to run and post process the numerical results.

## 4.3 Approach

*UTRC Phase field model:* The UTRC phase field model was based on the approach by Kobayashi [41]. In this model, the derivation of the evolution of the order parameter is geometrically motivated and is based on the Gibbs-Thompson formulation that relates interface normal velocity with the solidification temperature, liquidus slope and the interface curvature. The anisotropy of the solid-liquid interfacial energy is incorporated into the evolution equation through a cosine function that provides a four-fold symmetry to the interfacial energy as a function of the deviation of the dendrite orientation from the [100] directions that represent easy growth directions for cubic materials. The strength of the anisotropy is varied through an additional parameter that scales the magnitude of the interfacial energy with dendrite orientation. Extension of the model to three-dimensions (3-D) required incorporation of a 3-D anisotropy function where the interfacial energy was varied as a function of the orientation of the normal to the dendrite-liquid interface. The evolution of the concentration equation in the UTRC model is based on solving a time-dependent diffusion equation. An important feature in the model is the dependence of the partition coefficient on the interface velocity based on a kinetic correction proposed by Aziz and Kaplan [42]. In order to handle a moving heat source typical of AM, additional terms that relate the velocity of the heat source to spatial gradients in the order parameter and concentration were added to the right hand side of the evolution equations corresponding to a stationary heat source.

While the UTRC model was specifically developed for a pseudo-binary approximation of alloy 718 where all the solutes were lumped to a single secondary “element” and with an assumption of a linear liquid, the model cannot be easily extended to physically model a real alloy system with more than one actively partitioning solute and non-linear liquidus. Moreover, the UTRC model used normalized parameters with arbitrary values for some of the model parameters.

*Strategy:* Given the above constraint with the UTRC model, and with the long-term objective of being able to utilize phase-field simulations in the design of AM alloys where it is required to link the phase field simulations realistically with the alloy thermodynamics using physically relevant model parameters, it was decided to divide the effort between the two codes as follows:

1. Use LLNL phase-field code (AMPE) to incorporate the UTRC model and compare the two simulation results; use AMPE to perform 3-D simulations of multiple dendrite growth using the UTRC model
2. Use ORNL phase-field code (MEUMAPPS) along with an extension of the Kim-Kim-Suzuki model [43] to a ternary alloy to perform 3-D simulations of multiple dendrite growth, thermodynamically linking the simulations to a model ternary alloy that has the same solidification characteristics as IN 718

A brief description of AMPE and MEUMAPPS at the start of the project follows.

*MEUMAPPS:* The ORNL code, MEUMAPPS, at the start of the project was essentially focused on simulating solid-state transformations. Due to the small length scale of the simulation volume it was reasonable to assume isothermal conditions that allowed the use of periodic boundary conditions for the temperature, concentration and order parameter fields. Therefore, the governing phase field equations – Ginzburg-Landau equation for the time evolution of the multiple non-conserved order parameters, and Cahn-Hilliard equation for the time evolution of the conserved solute concentration field, were solved using a semi-implicit Fourier spectral method [44]. However, in AM conditions, steep temperature gradients exist at the solidification conditions even in microscopic volume elements and therefore periodic boundary conditions cannot be used. Therefore, the numerical approach for solving the governing equations had to be modified. Although the code had the capability to handle anisotropic interfacial energy between the matrix and the precipitates, the form of anisotropy in solidification simulations was significantly different and therefore further modification was required. The code had a framework for calculating the thermodynamic driving force for transformations through free energy functions obtained by fitting polynomials to thermodynamic calculations. However, a more general Calphad based thermodynamic module had to be developed in order to accurately describe the free energy of the solid and liquid as a function of composition and temperature, especially for alloys containing strongly partitioning solutes(s) such as Nb in IN 718.

*AMPE:* In the LLNL code called AMPE [45, 46], a finite volume approach is used to discretize the order parameters, orientation and concentration fields, and an implicit time integration is used to solve the evolution equations in a fully coupled manner using adaptive time-stepping and an iterative linear solver. A unique feature of the AMPE code is the introduction of the grain orientation evolution parameter through quaternions, that allows carrying just one order parameter for the two-phase, solid-liquid coexistence problem as in solidification, while different solid grain (dendrite) orientations are represented through the quaternions. The phase field model is also based on the Kim-Kim-Suzuki approach [43]. At the beginning of the project, the code had been used to simulate the growth of spherical solid seeds growing in an undercooled liquid in binary alloys, and it lacked the solid-liquid interfacial anisotropy required to simulate dendritic growth.

The project schedule and deliverables are as shown below.

					Year 1											
Tasks	description	UTRC	ORNL	LLNL	1	2	3	4	5	6	7	8	9	10	11	12
1	Modify ORNL and LLNL PFM codes to handle AM solidification problems	x	x	x												
2	Simulate benchmark ternary alloy problem and compare performance and scaling		x	x												
3	3D demonstration of microstructure solidification in AM		x	x												
4	Validation against UTRC experiments	x	x	x												

One of the capabilities of MEUMAPPS that was enhanced during the course of the project is the integration of the code with Calphad based thermodynamic model for the alloy. As part of this effort, a model Ni-Fe-Nb ternary alloy was designed to represent the multi-component Ni-base alloy IN 718 such that both alloys had the same equilibrium solidification range. This is an important characteristic of the alloy that has a direct bearing on the extent of constitutional undercooling in the liquid under given solidification conditions given by  $G$  and  $R$ , where  $G$  is the temperature gradient in the liquid and  $R$  is the interface velocity. The extent of constitutional undercooling determines whether the alloy solidifies in the columnar or dendritic mode under a given  $G$  and  $R$ . The excess thermodynamic free energy was calculated through Redlich-Kister polynomials for the solid and liquid phases obtained from the Gibbs free energy modules in Thermocalc™ for the Ni-Fe-Nb alloy. The enthalpy of the liquid and solid phases was obtained from the Gibbs free energy through the Gibbs-Helmholtz equation and the temperature and composition-dependent specific heats of the solid and liquid were obtained from the derivative of the enthalpy with respect to the temperature. The specific heat and enthalpy were used in the heat transfer equation required for coupling of MEUMAPPS with AM process-specific thermal boundary conditions to drive the microstructure evolution.

#### 4.4 Results

##### Simulations using MEUMAPPS:

*Modifications / Enhancements:* Initial approaches involved the use of Chebyshev collocation methods for handling non-periodic BCs, and attempts to embed a non-periodic domain in a larger domain with periodic BCs. However, these approaches were not successful because of the complex three-dimensional nature of the problem and numerical complexities involved in handling complex thermal BCs associated with AM.

Therefore, it was decided to use a semi-implicit, finite-difference approach in real-space that allowed the incorporation of general, time and space-dependent thermal flux boundary conditions. Evolution equations were set up for temperature, solute concentration and order parameter fields and the solution of resulting system of equations was carried out using a conjugate gradient method with diagonal preconditioning. The semi-implicit scheme assumed equal diffusion coefficient of the solutes in the solid and liquid side of the interface. These simulations were used to demonstrate the utility of large, massively parallel phase-field simulations to capture the growth of multiple dendrites in two- and three-dimensions. High performance computing strategy was based on subdividing the computational domain among large number of processes. Finite difference calculations required information from first nearest neighbors, which can lie on another process. Data exchange routines based on the message passing interface (MPI) were developed to facilitate efficient communication among processes. Sparseness of the coefficient matrix was exploited to limit storage and speed up matrix-vector multiplication required for solving the system of equations. In solidification problems, the solute diffusivity in the liquid is three to four orders of magnitude higher than in the solid. The introduction of such significant differences in solute diffusivity resulted in serious slowdown in solution convergence as well as significant errors related mass conservation. Therefore, the approach had to be changed once again. The final numerical approach that appears to work satisfactorily on a wide range of material and process parameters and the use of complex thermal boundary conditions associated with AM is the use of explicit finite difference.

*Introduction of solid-liquid interfacial anisotropy:* Simulating the solidification of metallic alloys requires incorporation of the anisotropy in the solid-liquid interfacial energy in the Ginzburg-Landau equation. In the case of 2-D simulations the anisotropy in the interfacial energy is introduced through a cosine function that results in the four-fold symmetry of the dendrite in cubic materials. The evolution of the dendrite is further influenced by a parameter that determines the strength of the anisotropy. MEUMAPPS code was modified to incorporate the anisotropy initially in 2-D and later in 3-D using a model adapted from the literature [47, 48]. While the disorientation between dendrites was represented by a single disorientation angle in 2-D, a rotation axis and a rotation angle pair were used to specify the dendrite orientation in 3-D, and the variation of interfacial energy normal to the s-l interface for an arbitrary orientation was calculated using a rotation matrix relative to a global coordinate system.

*Development of a ternary model alloy:* A model ternary alloy Ni-50wt%Fe-5wt%Nb was selected that approximates the solidification characteristic of the Ni-base superalloy IN 718. The equilibrium solidification range of IN718 was first determined by using a nominal composition of the alloy. Then the equilibrium solidification range for several reduced alloy combinations were calculated in order to find an alloy that would have the same solidification range as IN718. It was found that the presence of Fe and Nb are necessary in order to match the solidification range of IN 718. The calculations were performed using the commercial thermodynamics code Thermocalc<sup>TM</sup> using the Ni-base alloy database TTNi8.

*Integration of MEUMAPPS with alloy thermodynamics:* This effort required the evaluation of Redlich-Kister polynomials for the Ni-Fe-Nb system from the Gibbs energy module of the Thermocalc<sup>TM</sup> database. The thermodynamic driving force at each mesh point in the simulation domain is given by the free-energy difference between the solid and liquid at the given temperature, composition and the order parameter values. In the Kim-Kim-Suzuki [43] model, the free energies are described in terms of the concentrations of the species at the diffuse interface that are defined by equality of chemical potential. The calculation of the interface concentrations at every mesh point is done using a Newton-Raphson technique that incorporates equality of chemical potential of a given species at the diffuse interface. The enthalpy of the liquid and solid-phases were obtained from the Gibbs free energy through the Gibbs-Helmholtz equation, and the temperature and composition-dependent specific heats of the solid and liquid were obtained from the derivative of the enthalpy with respect to the temperature. The specific heat and enthalpy used in the heat transfer equation required coupling of MEUMAPPS with AM process-specific thermal boundary conditions to drive the microstructure evolution. A user subroutine has been developed,

tested and integrated with the MEUMAPPS code. The equations used in MEUMAPPS are provided in Appendix A.

*Simulations:* With the modifications described above in place, simulations of dendritic solidification in the model Ni-Fe-Nb ternary alloy were carried out in stages, beginning with single dendrite in 2-D using simple boundary conditions to simulations of multiple dendrites in 3-D using the complex, time-dependent boundary conditions provided by UTRC based on their larger length scale continuum simulations of heat transfer and fluid flow. Figure 1 shows simulations of multiple-dendrites in 2-D in the Ni-Fe-Nb model ternary. The simulation parameters are shown in Table 1.

Table 1: Simulation parameters used in 2-D simulations

Parameter	Value
Composition	Ni-0.50Fe-0.05Nb (mass fraction)
Edge boundary conditions: bottom, top, left, right	Dirichlet, Dirichlet, Neumann, Neumann
Initial Temperature	1570K
Bottom Temperature	1580K
Top Temperature	1560K
Thermal diffusivity	$7.0 \times 10^{-13} \text{ m}^2/\text{s}$
Specific Heat	720 J/mK
S-L interfacial energy	$0.05 \text{ J/m}^2$
Mesh resolution	$1.0 \times 10^{-8} \text{ m}$
Width of diffuse boundary	$5 \times 10^{-8} \text{ m}$
Solute diffusivity in solid or liquid	$10^4 \exp(-24000/T) \mu\text{m}^2/\text{s}$
Boundary mobility	$1 \times 10^{-7} \text{ m}^3/\text{Js}$
Strength of interfacial anisotropy	0.04
Simulation size	3000 x 3000 mesh points ( $30 \mu\text{m} \times 30 \mu\text{m}$ )

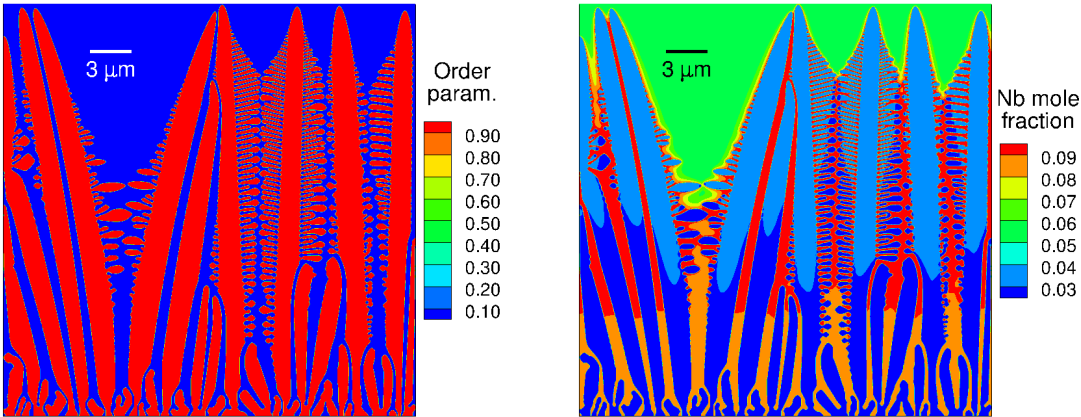


Figure 1. Two-dimensional phase field simulation performed using the thermodynamic model developed for Ni-Fe-Nb alloy to test the thermodynamic model and the anisotropic interfacial energy implementation in MEUMAPPS. Simulations took roughly 12 hrs. using 512 processes in a Cray XC30 cluster.

Multiple seeds were placed in the bottom edge and the growth temperature was in the temperature range 1560K – 1580K. A negative temperature gradient of  $0.67 \text{ K}/\mu\text{m}$  was used with no latent heat evolution. The simulations were carried out using a semi-implicit scheme using equal solute (Nb and Fe) in the solid

and the liquid. The simulations are able to capture the formation of secondary arms and Nb segregation between the primary and secondary dendrite arms.

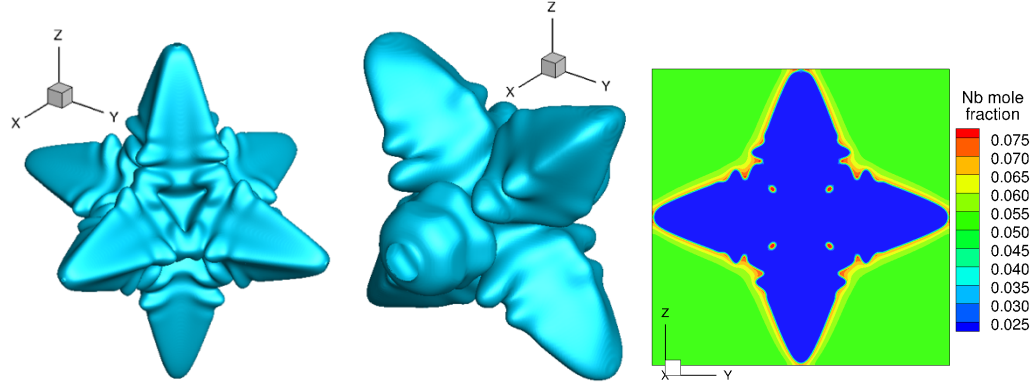


Figure 2. Simulation of 3-D dendrite in Ni-50%Fe-5%Nb alloy under isothermal conditions using MEUMAPPS showing nucleation and growth of dendrite in the standard orientation (left), random orientation (middle) and Nb distribution in a 2-D section through the dendrite (right). Simulations carried out using 4096 processes in a Cray XC30 cluster.

The simulations were then extended to 3-D by implementing the s-l interfacial anisotropy in 3-D. Simulations of a single equiaxed dendrite in a Ni-Fe-Nb alloy is shown in Figure 2. The simulations show the ability of the code to simulate the nucleation and growth of a dendrite with an arbitrary orientation required for the next step of simulating multiple dendrites in 3-D. While in 2-D the misorientation between two dendrites is simply described by a single rotation angle, in 3-D, it is described by a rotation axis and a rotation angle about the axis or a rotation matrix, as shown in Appendix A.

The single dendrite simulations were then extended to the growth of multiple dendrites in a temperature gradient using the Ni-Fe-Nb ternary as shown in Figure 3. Nuclei were introduced in the bottom surface of the simulation box whose size was  $4 \mu\text{m} \times 4 \mu\text{m} \times 10 \mu\text{m}$  with a spatial resolution of  $1 \times 10^{-8} \text{ m}$ . The simulations show the growth of the 3-D dendrites in arbitrary orientations with the formation of secondary arms. The above 3-D simulations assumed that the solute diffusivities are the same in the solid and liquid. Based on the parameters shown in Table 2, a negative temperature gradient of  $1.0 \text{ K}/\mu\text{m}$  was imposed with no latent heat of evolution.

Table 2. Parameters used 3-D phase field simulations

Parameter	Value
Composition	Ni-0.50Fe-0.05Nb (mass fraction)
Surface boundary conditions: left, right, front, and back	All Neumann with zero flux
Boundary condition: bottom and top	Dirichlet
Initial Temperature	1600K
Bottom Temperature	1605K
Top Temperature	1595K
Thermal diffusivity	$7.0 \times 10^{-13} \text{ m}^2/\text{s}$
S-L interfacial energy	$0.05 \text{ J}/\text{m}^2$
Mesh resolution	$1.0 \times 10^{-8} \text{ m}$
Width of diffuse boundary	$5 \times 10^{-8} \text{ m}$
Solute diffusivity in solid or liquid	$5.6 \times 10^{-4} \exp(-286000/RT) \text{ m}^2/\text{s}$
Boundary mobility	$4 \times 10^{-5} \text{ m}^3/\text{Js}$
Strength of interfacial anisotropy	0.04

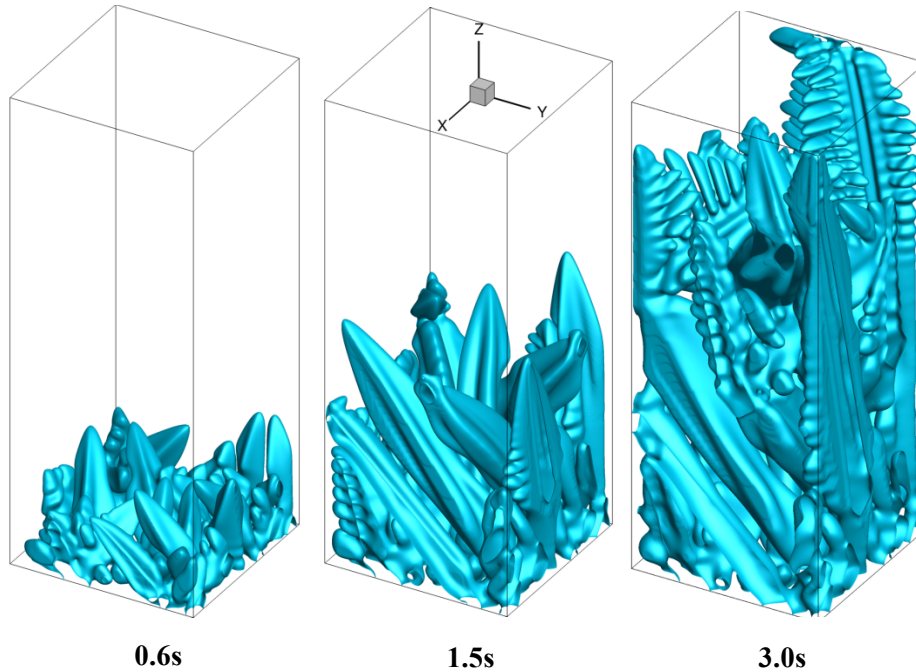


Figure 3. MEUMAPPS simulations of 3-D dendrites in Ni-Fe-Nb alloy. Nucleation and growth of multiple dendrites in a temperature gradient was simulated using 4096 processes in a Cray XC30 cluster. Simulation volume  $4 \times 4 \times 10 \mu\text{m}^3$ .

Review of literature of solidification of IN 718 indicates that the solute diffusivity in the liquid is of the order of  $10^{-9} \text{ m}^2/\text{s}$  over a wide solidification temperature range. However, the diffusivity of solute in the solid decreases significantly with temperature during solidification and it can be several orders of magnitude smaller than in the liquid. This is responsible for the coring that is observed in as-solidified dendrites. However, this effect is not captured in the above simulations. As mentioned previously, introducing orders of magnitude difference in the diffusivities resulted in numerical issues with the semi-implicit method. Therefore, for subsequent simulations that involve using real thermal fluxes associated with additive manufacturing, an explicit finite-difference technique was used to solve the evolution equations involving order parameter, concentration and temperature.

*Simulations using explicit finite-difference technique:* Before performing simulations under AM conditions, pseudo-3D simulations were performed using simple boundary conditions where Neumann boundary conditions with zero flux were imposed on all the external surfaces, except the  $z=0$  surface where varying magnitudes of flux were applied to establish different temperature gradients along the growth direction. The simulations were used to (1) verify that the explicit finite difference approach will be able to handle a wide range of heat flux boundary conditions, (2) capture the effect of temperature gradient on the solidification morphology, (3) test the latent heat model for the Ni-Fe-Nb ternary alloy obtained using Calphad approach. The parameters used in the simulations are shown in Table 3.

Table 3. Phase field parameters used for explicit finite difference simulations

Parameter	Value
Simulation box size	600 x 2 x 600 mesh points
Composition	Ni-0.60Fe-0.031Nb (mass fraction)
Surface boundary conditions: left, right, front, back, top	All Neumann with zero flux
Surface boundary condition bottom ( $z=0$ )	Neumann with three different flux magnitudes

Initial Temperature	Gradient in Z direction from 1650K at Z=0 to 1700K at Z=600
Thermal conductivity	30.0 W/mK
Specific Heat	Calculated using Calphad model
S-L interfacial energy	0.1 J/m <sup>2</sup>
Mesh resolution	2.0 x 10 <sup>-8</sup> m
Width of diffuse boundary	1 x 10 <sup>-7</sup> m
Solute diffusivity in liquid	2.58 x 10 <sup>-8</sup> m <sup>2</sup> /s
Solute diffusivity in solid	5.6 x 10 <sup>-4</sup> x exp (-286000/RT) m <sup>2</sup> /s
Phase field mobility	4 x 10 <sup>-1</sup> m <sup>3</sup> /Js at 1600K
Strength of interfacial anisotropy	0.06

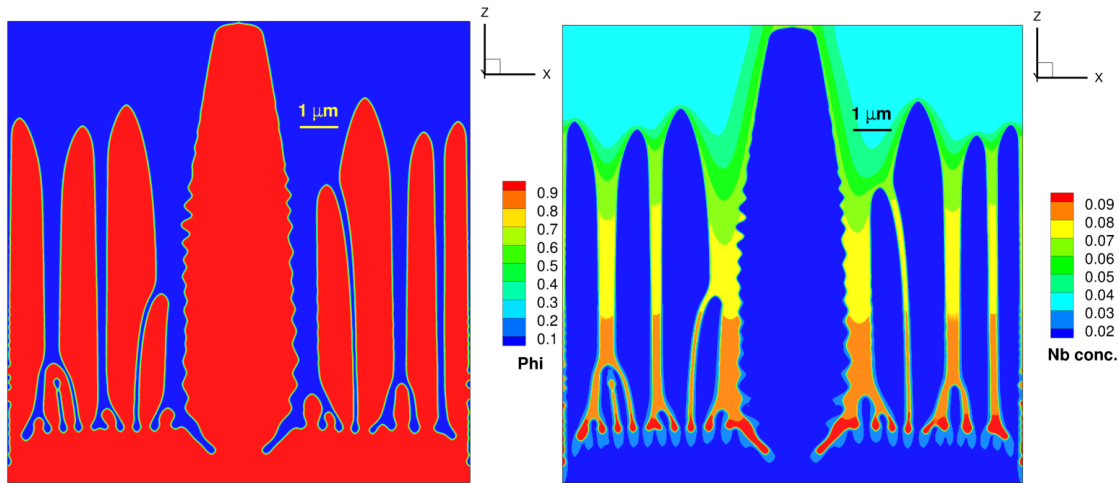


Figure 4: Solidification in a columnar-dendritic mode with a temperature gradient of  $8 \times 10^6$  K/m normal to  $z=0$  surface. Contours of order parameter showing morphology of columnar dendrite (left) and Nb concentration profile showing Nb enrichment in the interdendritic liquid (right).

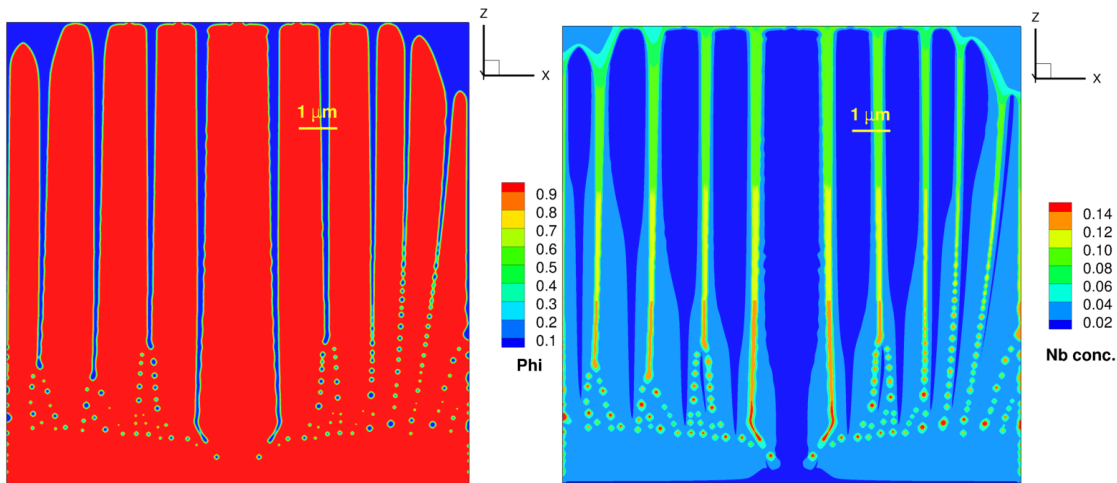


Figure 5: Solidification in a columnar-dendritic mode with a temperature gradient of  $2 \times 10^7$  K/m normal to  $z=0$  surface. Contours of order parameter showing cellular morphology with no indication of secondary arm formation (left) and Nb concentration profile showing Nb enrichment in the liquid between the cells (right).

The phase field mobility was assumed to have an Arrhenius relationship with an activation energy half that of solute diffusivity in the bulk. Figure 4 shows that a columnar dendritic morphology is obtained using the parameters shown in Table 4 with a temperature gradient of  $8 \times 10^6$  K/m at the bottom surface. The applied temperature gradient acts to extract the heat in the  $-z$  direction, causing a positive temperature gradient in the liquid. A single seed was placed at the center along the  $z=0$  surface and the latent heat of solidification is evolved at each mesh point as the volume fraction of solid (order parameter) evolves due to solidification. When the temperature gradient at  $z=0$  is increased to  $2 \times 10^7$  K/m, the solidification morphology changes to a cellular structure as shown in Figure 5. The Nb segregation between the cells shown in Figure 5 is in general higher than the interdendritic Nb segregation shown in Figure 4. With the higher heat extraction, the bottom surface cools faster and the solid-liquid interfacial temperature is lower, with a higher partitioning of Nb into the liquid.

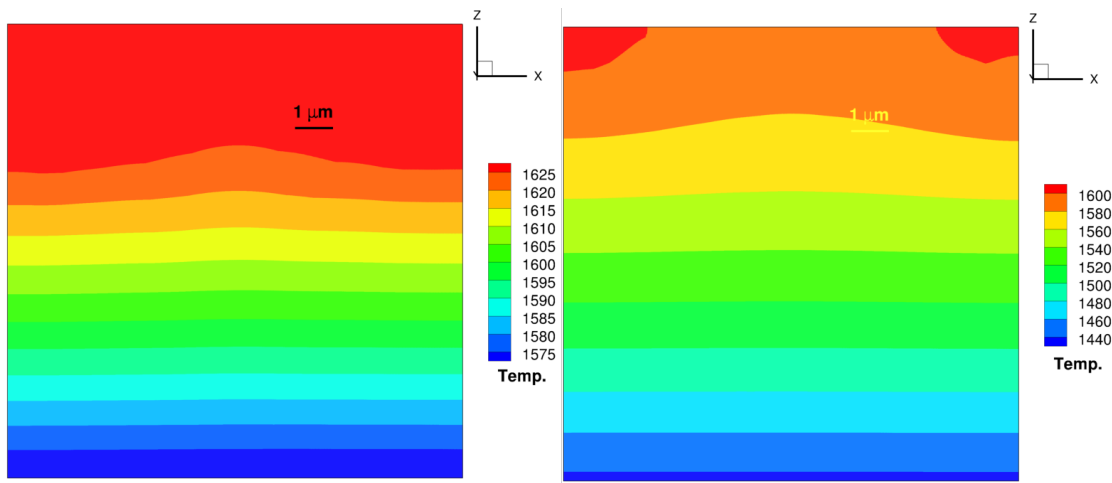


Figure 6. Temperature distribution at the end of solidification for a temperature gradient normal to  $z=0$  surface of  $8 \times 10^6$  K/m (left), and  $2 \times 10^7$  K/m (right) corresponding to solidification morphologies shown in Figs. 4 and 5, respectively.

The temperature distribution for the solidification conditions shown in Figs. 4 and 5 are shown in Figure 6. The temperature gradient increases and the bottom and top temperatures decrease with increasing flux. The temperature contours shown in Figure 6 also indicate that the latent heat of solidification at the moving s-l interface contributes to localized heating of the liquid in the immediate vicinity. The results indicate the capability of the explicit finite difference approach to handle thermal boundary conditions, and the capability of the Calphad based latent heat model. The results also indicate that the solidification morphology is sensitive to the thermal boundary conditions and the temperature gradients in the domain.

*Solidification Simulations under AM conditions:* In the following simulations, the thermal field that drives the phase field simulations is obtained from larger length scale continuum simulations of heat transfer that includes the energy input from the heat source, the heat source velocity, heat conduction in the solid and liquid portions of the melt pool and fluid flow in the melt pool. The thermal boundary conditions were provided by UTRC based on thermal modeling for a single track laser weld performed on 718 alloy plate. The thermal boundary conditions were provided as face-averaged temperature gradient values as a function of time for the six-faces of a 3-D volume whose length scale is much smaller than that of the melt pool. Typical thermal boundary conditions obtained from UTRC for a  $33.4 \mu\text{m} \times 30 \mu\text{m} \times 25.2 \mu\text{m}$  volume are shown in Figure 7 and Table 4. The initial temperature distribution and the thermal boundary conditions were used to drive the phase field simulations using an explicit finite element technique for solving the evolution equations for the order parameter, concentration and temperature. The temperature gradients (negative of the heat flux) shown in Table 4 indicate that the fluxes normal to the  $y$  direction are very small compared to those normal to the  $X$  and  $Z$  directions. Therefore, the solidification

morphology can be obtained using a pseudo 3-D approach by limiting the simulation thickness in the y – direction.

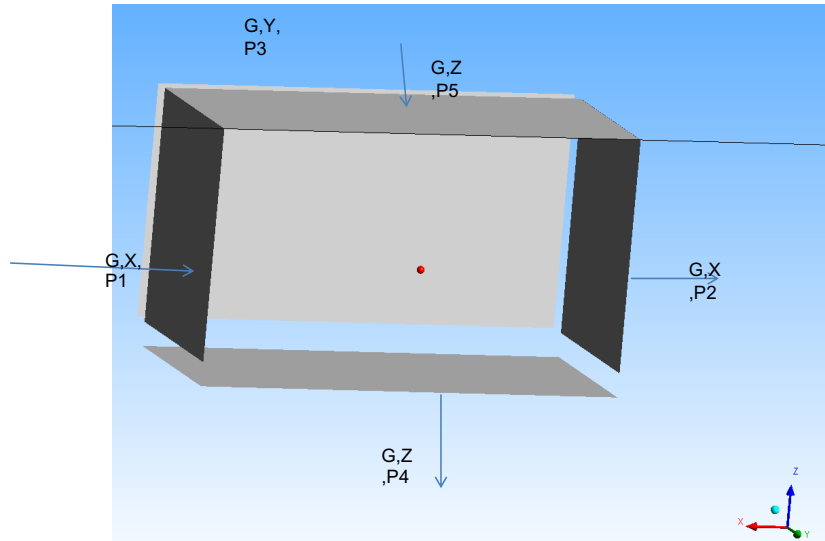


Figure 7. Schematic representation of the face-averaged, time-dependent thermal boundary conditions obtained from UTRC based on heat transfer simulations performed at larger length scale.

Initial simulations were carried out using the parameters shown in Table 3 along with the thermal boundary conditions given in Table 4 provided by UTRC. The objective was to determine the mode of solidification that corresponds to the UTRC boundary conditions for the same simulation volume as in Table 3. A single nucleus was placed at the center of the surface at  $Z=0$ . The results shown in Figure 8 indicate that the solidification mode is in a stage of transition from cellular to cellular-dendritic under these thermal boundary conditions.

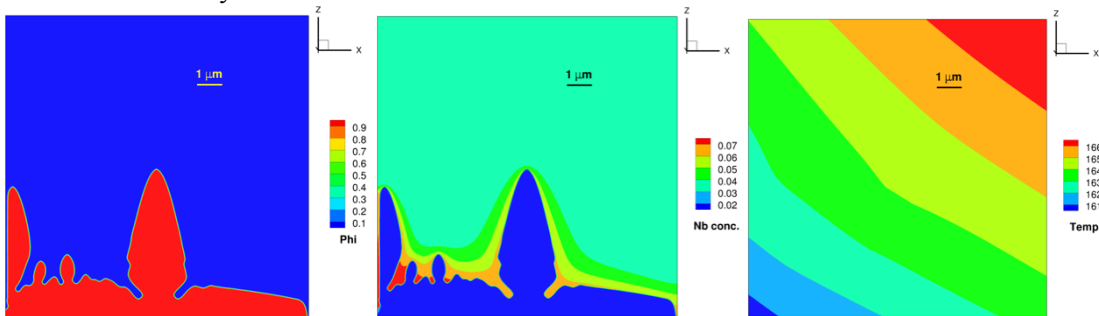


Figure 8. Evolution of the order parameter (left), Nb concentration (middle) and temperature distribution (right) using thermal boundary conditions shown in Table 4 and the same simulation volumes used in Figures 5 and 6.

Figures 9-11 show the solidification morphology obtained using the thermal boundary conditions provided by UTRC shown in Table 4 but with different sets of initial temperature conditions. All three simulations were carried out using the X and Z dimensions shown in Figure 4 ( $33.4 \mu\text{m} \times 25.2 \mu\text{m}$ ), but with a thickness of just 2 mesh points in the y-direction to perform a pseudo-3D simulation. Figure 9 shows the solidification morphology obtained when the initial temperature distribution in the domain varied from 1650K at  $Z=0$  to 1700K at  $Z=1260$  (top surface). Therefore, all the mesh points are above the bulk liquidus temperature of 1650K for alloy 718 as determined in Thermocalc™. The imposed initial temperature gradient is artificial and it is assumed to adapt very quickly to the thermal boundary conditions due to the very high thermal diffusivity compared to phase field mobility. Multiple seeds were

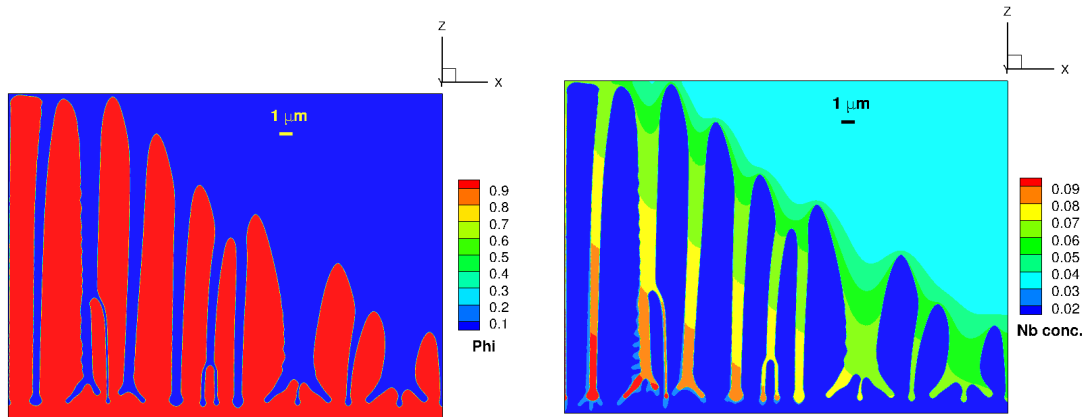


Figure 9. Evolution of order parameter and Nb concentration based on the simulation parameters listed in Table 3, but the simulation size in the X and Z directions matching the UTRC model and with a thickness of 2 mesh points in the Y-direction (pseudo-3D). The structure is essentially columnar with a slight indication of secondary arm formation.

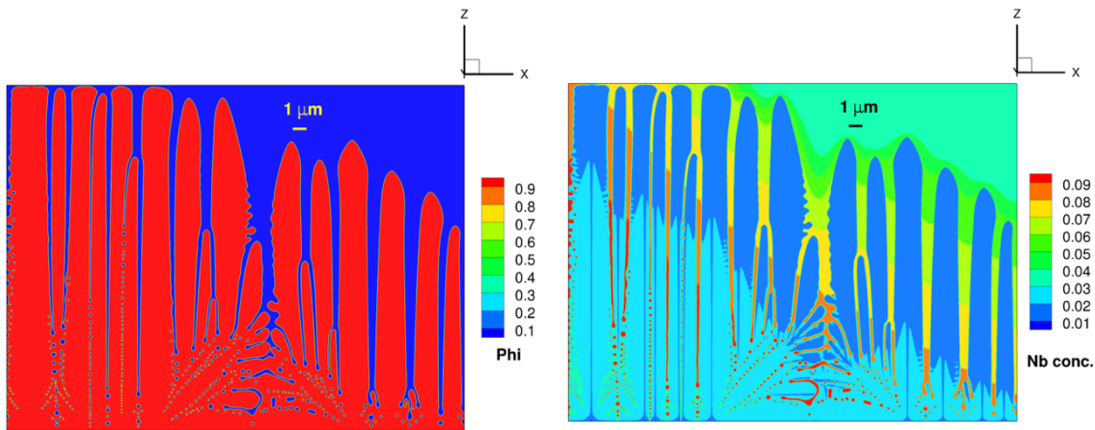


Figure 10. Solidification morphology obtained using pseudo-3D simulations with UTRC initial temperature distribution and thermal boundary conditions

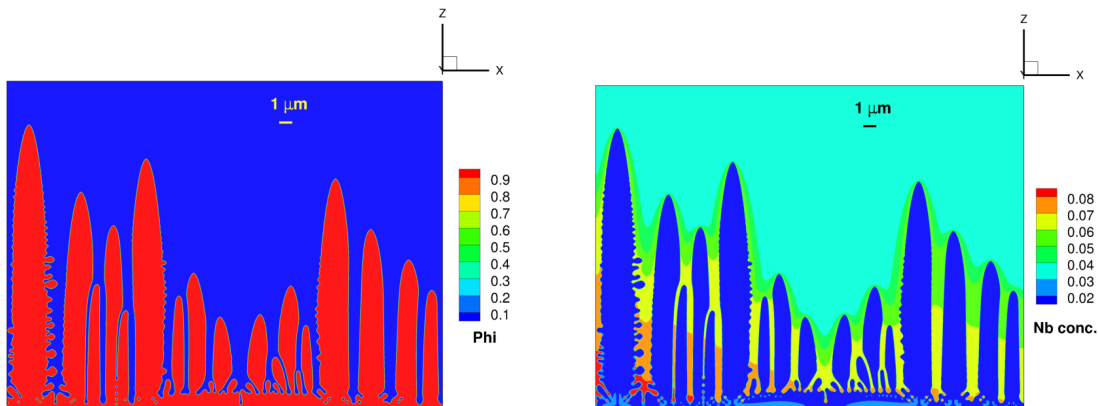


Figure 11. Solidification mode obtained when the UTRC thermal boundary conditions are used with an initial liquid temperature of 1580K. The order parameter (left) and Nb distribution (right) indicate clear formation secondary arms

placed at the  $z=0$  surface. It can be seen from Figure 9 that the solidification structure is essentially columnar with a primary arm thickness of about 2.0 to 3.0  $\mu\text{m}$ . There is a slight indication of secondary

arm formation in a few cells, with a secondary arm thickness of about  $0.5 \mu\text{m}$ . Figure 10 shows the solidification structure when the initial temperature distribution is mapped from the values provided by UTRC. The initial temperature ranged from 1425K to 1610K. Seeds with an orientation spread were introduced at  $Z=0$ . The solidification morphology again shows indication of transition from columnar to columnar-dendritic morphology for the initial and boundary conditions provided by UTRC. The thickness of the secondary arms is again roughly  $0.5 \mu\text{m}$ . Figure 11 shows the solidification morphology when the initial temperature is specified as 1580K for the entire domain. Compared to Figs. 9 and 10, the tendency for dendrite formation is the greatest under this initial condition. However, there is no change in the dimensions of the primary or secondary arms compared to those in Figs. 9 and 10. Figure 12 shows 3D

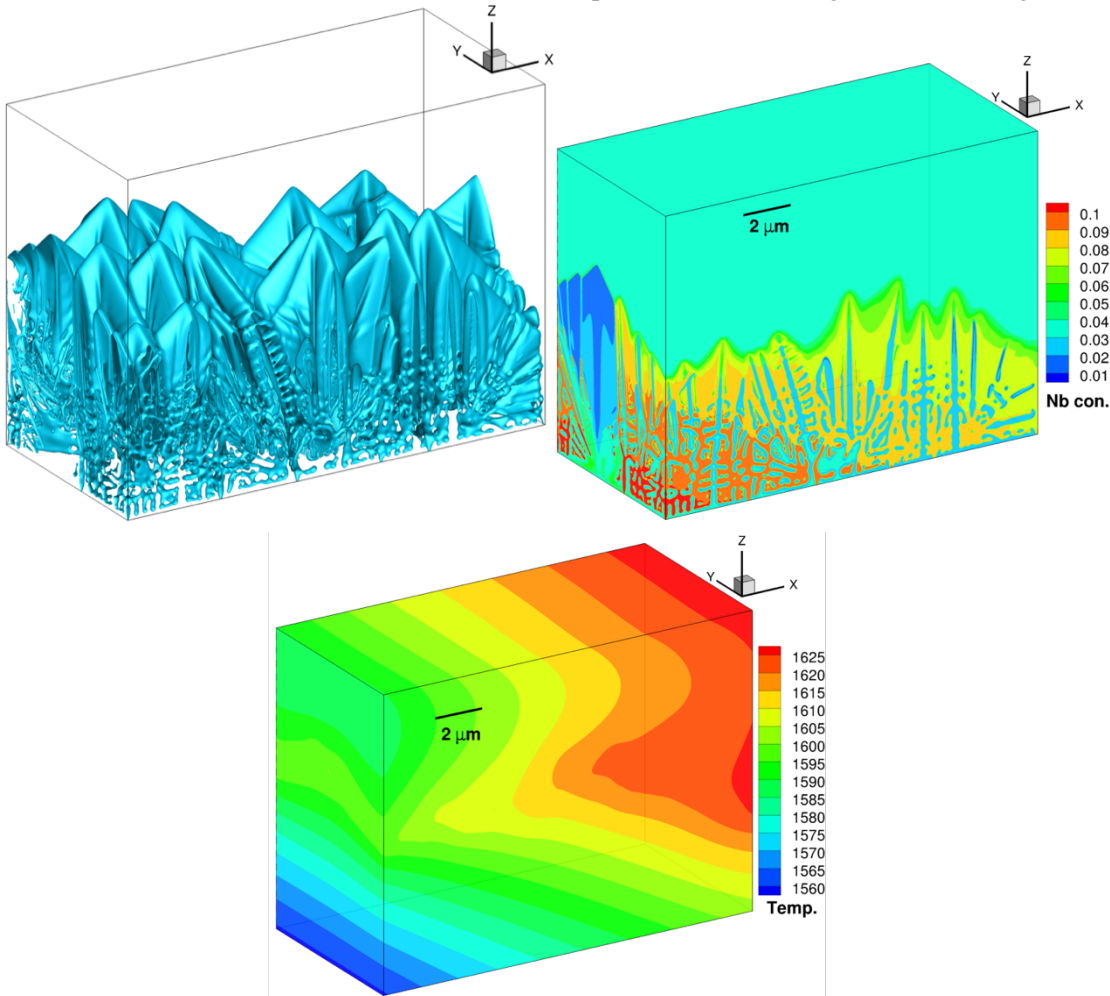


Figure 12. Simulation of multiple dendrite evolution in 3-D using UTRC thermal boundary conditions. Simulations using 4096 processes in a Cray XC30 supercomputer. The order parameter isosurface plot (top left) and contours of Nb concentration (top right) show indications of dendrite formation. The bottom figure shows the temperature distribution at the end of the simulation.

solidification microstructure of multiple dendrites using UTRC boundary conditions. Seeds with an orientation spread were placed at the  $Z=0$  surface and the initial temperatures specified by UTRC were used (same as in Figure 10). The simulations took 24 hours using 4096 processors in a Cray X30 cluster. Once again there is evidence of transition from columnar to dendritic transition with a secondary arm thickness of about  $0.5 \mu\text{m}$ . **Figure 12 is a demonstration of the project milestone of simulating multiple dendrite growth in 3D using thermal boundary conditions provided by a continuum code.**

### Simulations using AMPE:

*Modifications / Enhancements:* To carry out the investigations described in this report using AMPE, several features had to be added to the code. The following list describes the main additions to the code:

- Implemented Beckermann's model for composition time-evolution based on binary partition coefficient  $k$
- Implemented anisotropic interfacial energy (2D and 3D)
- Implemented UTRC specific model for phase variable time-evolution
- Added capability to compute solidification front velocity based on derivatives of phase variable

Various design changes had to be done to integrate these new features within AMPE and preserve the correctness and performance of models previously implemented.

*Model verification and numerical issues:* Based on the proposal goals, the first main task on the LLNL side was to implement the UTRC phase-field model into LLNL code AMPE [45, 46], with the subsequent related task of verifying that AMPE and the COMSOL implementation of the UTRC model were leading to the same numerical results. While doing that, the following issues were encountered:

- A mesh spacing of 0.3 was used in the original work [39]. It turns out this resolution, while key to enable large 2D simulations on limited computer resources, was not sufficient to resolve adequately the phase-field model as parameterized for IN718. Based on the value of PFM parameters, the interface thickness for the liquid-solid interface can be estimated to be of the order of 0.01 (see for instance expression (16) in [49] with  $\varepsilon=0.01$  and  $W_A=0.5$ ). So, we would recommend using a mesh spacing of 0.002 to properly resolve these interfaces.
- The UTRC team chose to use “normalized” equations, rescaling temperature, lengths, and time units by characteristic values of the problem, while AMPE used parameters with realistic dimensions in the original implementation. Trying to relate the dimensionless parameters with the corresponding dimensional parameters was challenging while trying to determine what parameters were potentially responsible for unwanted behavior of the model.
- In addition to the two issues above, some of the model parameters were not defined in [39] and in the documents shared by UTRC. Several discussions were held with UTRC that resulted in the formation of a smaller, well resolved test problem (rectangular 2D domain, solidifying from the bottom) that would allow a comparison between the two implementations. The UTRC team also shared their input file so that there was no confusion or translation errors in parameter values. After resolving the issues above, we were able to compare AMPE results with UTRC-COMSOL model and reach a state where we were quite confident both codes are solving the exact same equations. Obviously, our findings about mesh resolution meant that we had to reduce the scale of our simulations compared to our initial target.

*UTRC Phase-field Model:* The equations in the model proposed by UTRC were very similar to the equations proposed by Beckermann et al. in [46]. The only difference was in the driving force for solidification which, instead of being simply a linear function of the difference between the local temperature and the liquidus line as in [46], was modified in UTRC model to make it a smooth function with a maximum value that is reached asymptotically. This model was used by Beckermann et al. to study solidification in Al-4%Cu in isothermal systems. Table 5 shows the non-dimensional parameters used in the UTRC model in their COMSOL simulations and the AMPE input parameters required to reproduce the results of the UTRC model implemented in COMSOL. AMPE internal units are s for time, pJ for energies and  $\mu\text{m}$  for length scales. Input parameters are typically required in those units. There are a few exceptions for numerical reason. Unlike UTRC implementation in COMSOL, AMPE uses compositions between a and 1. It only affects the value of  $mL$  which has to be chosen 100x larger to compensate for that choice. Using the parameters proposed by UTRC, the phase-field simulations showed large regions near solid-liquid interfaces where the phase value has a “plateau” at  $\phi=0.5$ . This led to not well defined interfaces. This issue was also noticed in COMSOL results shared with us.

Name	Expression	Description
alpha	0.9	
delta	0.06	Anisotropy parameter
tau	3e-4	Inverse mobility
gamma	10	
Te	1	Melting T
epsilon	0.01	PFM parameter
K	2	L/Cp ratio
DI	1.647e-3	Diffusion coeff. in liquid
ke	0.48	Partition coeff. at equilibrium
Ds	1.647e-7	Diffusion coeff. in solid
mL	-0.0545	Liquidus slope
$\alpha_T$	1.	Thermal diffusivity coeff.

Name	Expression	Units	Description
alpha	0.9		
delta	0.06		Anisotropy parameter
$M_\phi$	1./3e-4	1/pJ s	Mobility
gamma	10		
Te	1	K	Melting T
epsilon	0.01	(pJ/ $\mu\text{m}$ ) <sup>2</sup>	PFM parameter
L	2		Latent heat
$c_p$	1.		Heat capacity
DI	1.647e-3	$\mu\text{m}^2/\text{s}$	Diffusion coeff. in liquid
ke	0.48		Partition coeff. at equilibrium
Ds	1.647e-7	$\mu\text{m}^2/\text{s}$	Diffusion coeff. in solid
mL	-5.45		Liquidus slope
$\alpha_T$	1.e-8	$\text{cm}_2/\text{s}$	Thermal diffusivity coeff.
Vm	1.e-6	$\text{m}^3/\text{mol}$	Molar volume
$\omega$	1./64.	pJ/ $\mu\text{m}^3$	Double well height

Table 5. Comparison of UTRC (left) and AMPE (right) model parameters

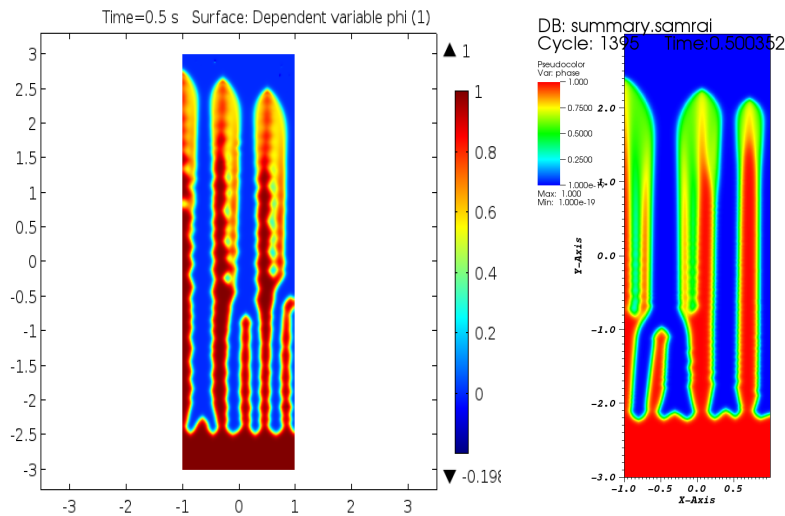


Figure 13: Comparison of COMSOL results (left) with AMPE results (right) on benchmark 2D problem. Differences can be explained by the different discretizations used by the two codes (Finite Elements Method vs. Finite Volumes)

While PFM in general relies on diffuse interfaces to make it a tractable method on a finite computational mesh, these “plateau” are undesirable. There is however a simple remedy, which is to raise the height of the double well potential. In this case, a 20% increase was sufficient and didn’t affect much other properties of the model. The improvement in the interface characteristics based on the suggested changes in parameterization is shown in Figure 14 using AMPE code. For the UTRC model in which that parameter did not appear explicitly, the equivalent operation was to increase the mobility by 20%, while reducing  $\epsilon$  and  $\alpha$  each by 20%. The suggested changes in parameterization were used by UTRC and it was found that the new parameters significantly improved the interface sharpness, although the partitioning of Nb at the s-l interface was still not very convincing. Figure 15 shows the results obtained by UTRC using their phase field model in COMSOL.

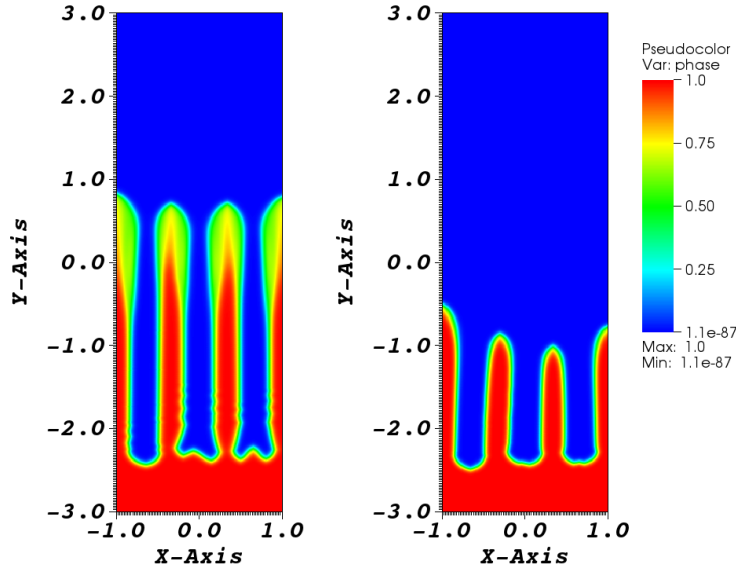


Figure 14: Comparison of results using original UTRC parameterization of the model (left) with new proposed parameterization (right) for the phase variable equation. Snapshots were taken at the same time of the evolution. Note the better defined interface on the right, as well as the different behavior.

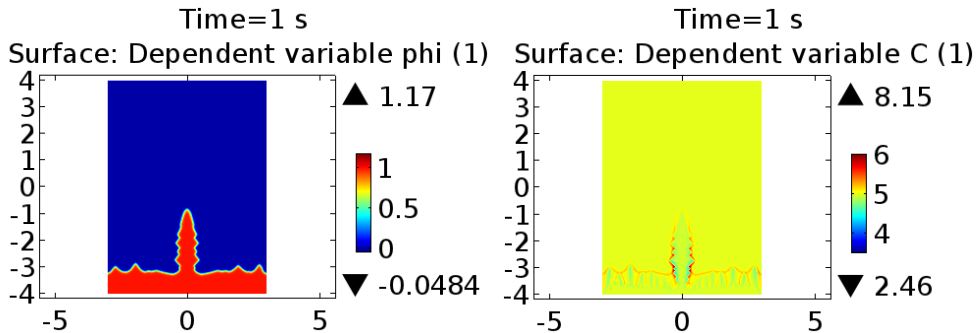


Figure 15. Appearance of the solid-liquid interface (left) and Nb concentration profile obtained by UTRC using the new model parameters suggested by LLNL

The other issue we found with this model was the lack of partitioning for the composition field. Actually, for the model as parameterized, there seemed to be a lack of coupling, or a very weak coupling, between the phase variable and the composition field. This issue was also noticed in COMSOL results shared with us. Going back to the work of Beckermann et al. [50] using a similar model, we notice two major differences: 1) Results published by Beckermann only included isothermal solidification. UTRC model is coupled to a diffusion time-evolution equation for temperature. 2) The kinetic coefficient  $\mu_k$  used for Al-4%Cu is about 3 orders of magnitude smaller than the coefficient in UTRC model. They actually make a comment (note attached to table 1 of [46]) that  $\mu_k$  was rescaled by a factor  $\sim 10^{-4}$  compared to its “physical” value due to the phase-field interface width being much wider than the real physical interface. Could it be that the  $\mu_k$  in UTRC model needed to be rescaled properly? After realizing these modeling issues, we carried out a series of simulations to try to understand better where the source of the problems was, and how the model could be better parameterized to simulate solidification in IN718 and possibly other materials.

- Scale up diffusion compositions by very large factor. This leads to partitioning, and a composition profile following the solidification front. We have however no physical justification for this model.
- Reduce kinetic coefficient  $\mu_k$  by large factor (as in [50]). Using a factor  $10^4$  as in [50], we observe a clear partitioning. For this test, we also modified slightly the model and replaced  $c_l$ , the liquid

composition, in the driving force term ( $T_m - T + m_1 c_1$ ) by  $c_0$ , the nominal composition. Results are shown in Figures 16 and 17. Note also that in this case, the phase-evolution equation is totally decoupled from the composition equation. But the different behavior seen in Figure 16 and 17 is mostly due to changes in time scales for the phase variable due to kinetic coefficient rescaling, while the temperature equation time scale has not changed.

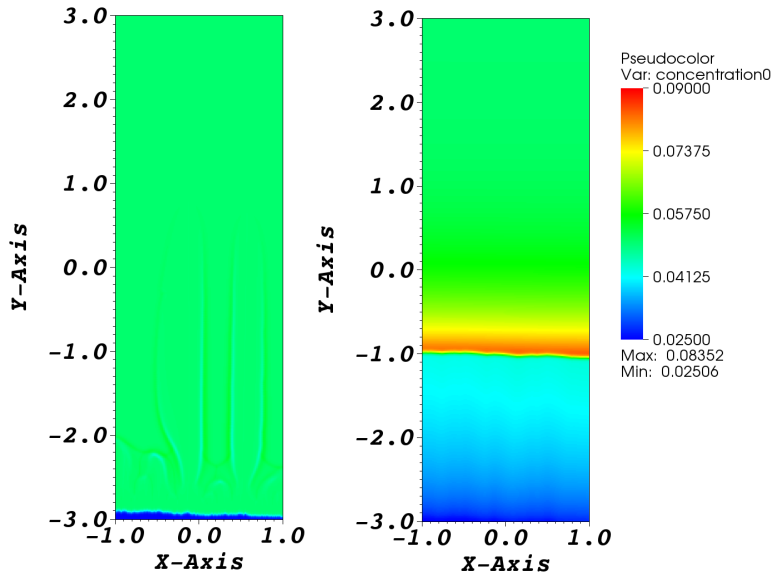


Figure 16: Composition field with kinetic coefficient from UTRC model (left) vs. rescaled coefficient as proposed by Beckermann (right). Partitioning is clearly visible with a rescaled kinetic coefficient, while the composition field remains essentially unchanged from the initial conditions with the UTRC model

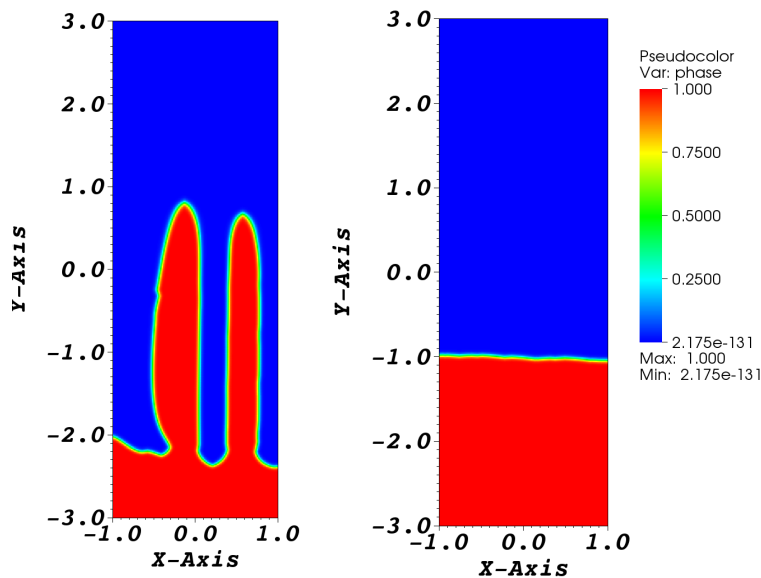


Figure 17: Phase variable corresponding to previous figure, using UTRC parameters at  $t=0.5$  (left) and after rescaling the kinetic coefficient at  $t=1000$

If we consider a completely different class of models, such as the Kim-Kim-Suzuki model [43] with CALPHAD parameterized free energy functions, a much stronger coupling between the phase variable and the composition variable can be obtained, and partitioning naturally appears (see ORNL approach described earlier).

**3-D Simulations:** By employing the proposed modifications to the UTRC parameters we were in a position to simulate the growth of multiple dendrites in 3-D. In figures 18-20, we present results of the solidification evolution simulated from AMPE. In these runs diffusion coefficients were set at values much higher than the ones presented in Table 5. The values selected for these demonstrative runs were  $D_l = D_s = 0.1647 \text{ } (\mu\text{m}^2/\text{s})$ . The system size was  $2 \times 6 \times 2 \text{ } \mu\text{m}^3$ . The runs were executed in Syrah platform of LC using 1024 processors. In these runs zero flux boundary conditions were imposed for concentration field, phase field and quaternion fields. For the temperature field, Neumann boundary conditions were imposed with very small gradient  $-10^{-2} \text{ } (\text{K}/\mu\text{m})$  on the sides along the X and Z-axis (lateral sides in the Figs) and on the top boundary along the Y-axis. At the bottom boundary along the Y-axis we imposed a temperature gradient  $-5 \text{ } (\text{K}/\mu\text{m})$ . With this set of boundary conditions, we mimic the situation of rapid solidification. [Note that the quaternion field was not used in these simulations. Parameters for the quaternion field are highly dependent on the other parameters of the phase-field model, in particular those describing the solid-liquid interfaces, and are not trivial to determine. Thus, it is important to fully determine all the other parameters carefully before carrying out this task. As described in this report, we have not reached a good set of PFM parameters yet for Beckermann's equations to properly model IN718, and thus calculations with quaternions have been put aside for now.

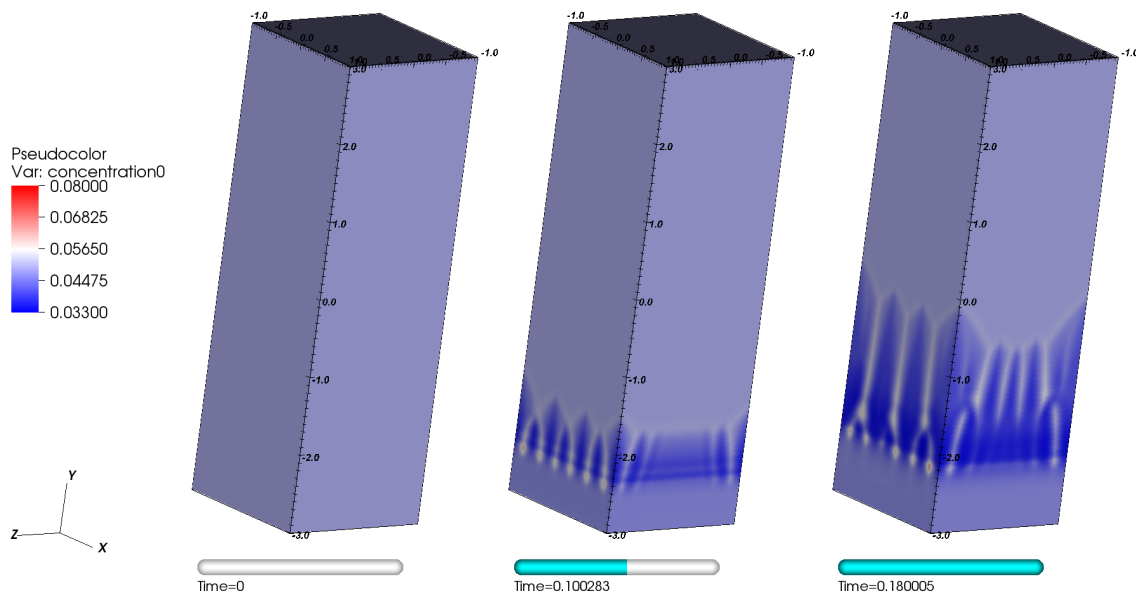


Figure 18. Three chronologically ordered snapshots of composition profile during dendritic evolution.

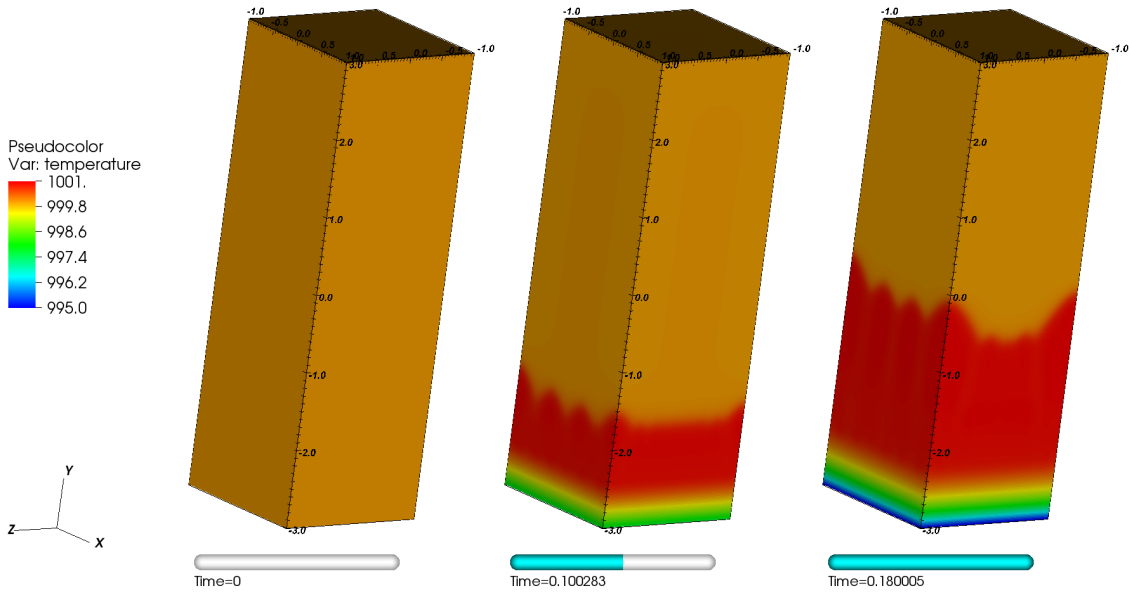


Figure 19. Evolution of temperature profile during solidification.

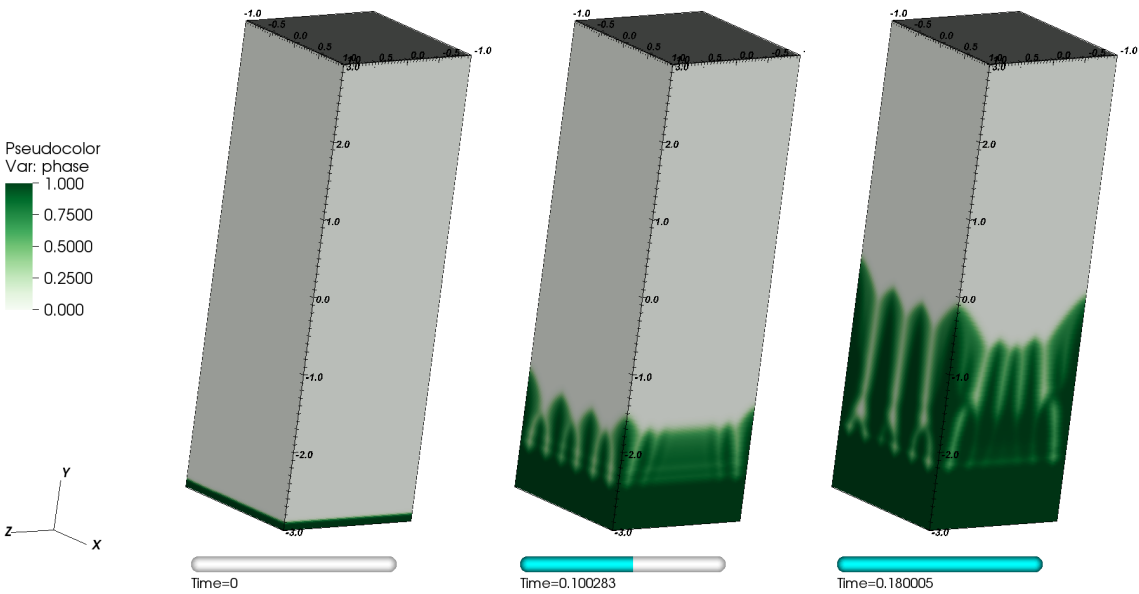


Figure 20. Evolution of phase field variable profile during solidification.

#### 4.4 Discussion

*Experimental Results:* Two sets of experimental results were provided by UTRC in order to validate the simulation results. The first set of results were based on [39] laser powder bed fusion (LPBF) processing of alloy 718. Typical dendritic structures, secondary arm spacing and Nb segregation are shown in Figure 21. From Figure 21 we can see that under the thermal history of the process, the resulting solidification

structure was essentially columnar dendritic, which a primary arm thickness of about 4  $\mu\text{m}$  and a secondary arm spacing of about 1  $\mu\text{m}$ . Significant Nb segregation was found in the interdendritic regions, with a peak Nb concentration of about 9 wt.%. The thermal boundary conditions corresponding to the LPBF process were available only for an irregular weld pool shape that could not be readily used as boundary conditions for phase field simulations because MEUMAPPS simulations were based on finite difference technique performed in a regular geometry. However, it is interesting to see that similar microstructural features are observed for the simulations shown in Figure 4 where zero-flux Neumann boundary conditions are imposed on all surfaces of the simulation volume except for the  $Z=0$  surface where a temperature gradient of  $8 \times 10^6$  K/m (corresponding to an outward heat flux at the boundary) is imposed. Note that when this temperature gradient is increased to  $2 \times 10^7$  K/m, essentially cellular microstructure was obtained as shown in Figure 5. The thickness of the primary arm is about 4  $\mu\text{m}$  and the secondary arm spacing is about 1  $\mu\text{m}$ , very close to what was observed experimentally. However, the secondary arms shown in Figure 4 are not well developed, showing that the structure represents a transition from a fully cellular to a columnar dendritic structure observed experimentally.

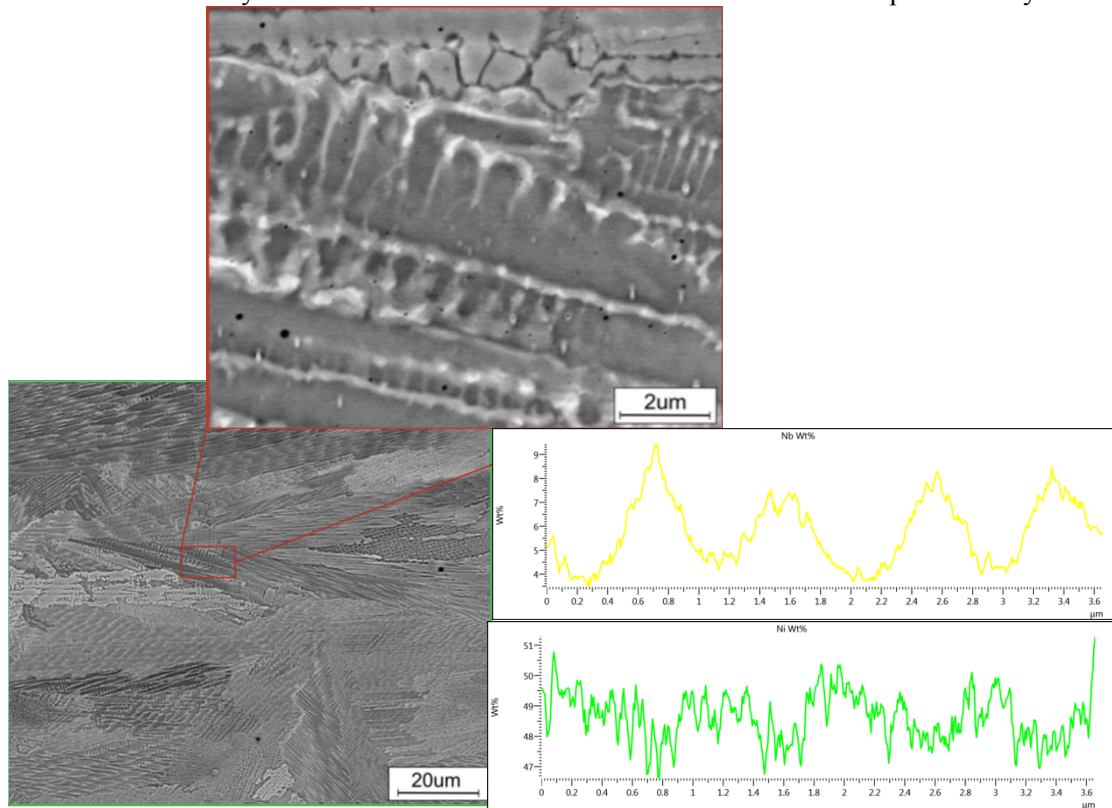


Figure 21. Dendrite morphology and Nb concentration profile obtained during LPBF processing of IN 718 [39].

The interdendritic Nb concentration shown in Figure 4 is in atom fraction that ranges from about 0.05 to 0.07, that corresponds to 0.08 to 0.11 wt. fraction Nb, somewhat higher than the values shown in Figure 21. In fact, in all of the simulations performed using the model Ni-0.031Nb-0.6Fe alloy (concentrations in atomic fraction), the Nb concentration in the inter-cellular / inter-dendritic regions was in the 0.08 – 0.11 in wt. fraction. The model Ni-Fe-Nb alloy was chosen as the ternary equivalent of the IN 718 with the same equilibrium solidification range. However, it is possible that this simplification resulted in a deviation of the liquidus surface that can result in an over prediction of the Nb concentration in the liquid. However, it must be added that in order to make a better comparison between the model predictions and

experimental Nb segregation, it is necessary to construct Nb maps rather than to rely on measurements performed along a single line.

Under AM conditions, a positive temperature gradient exists in the melt pool with the lowest temperatures at the s-l interface and the highest temperatures in the fully molten region. The magnitude of the gradient depends on the location of the microscopic volume element. For elements that lie along the major axis of the elliptical weld pool, the growth velocity of the s-l interface ( $R$ ) is the highest and the temperature gradient ( $G$ ) is the lowest and such a condition in general promotes the formation of a cellular-dendritic structure. However, for volume elements that lie along the minor axis of the weld pool, high  $G/R$  ratios exist in general that promote the formation of cellular structures. In addition, for a given location there is an added effect of the latent heat of evolution. The evolution of the latent heat at the s-l interface helps to reduce the steep positive temperature gradient in the liquid or even introduce a negative temperature gradient in the liquid at the s-l interface. Depending on the magnitude of the latent heat and the thermophysical properties of the alloy, it is possible that a location that is expected to solidify in the cellular mode may solidify in the cellular dendritic mode. According to solidification theory, the solidification mode depends on the extent of constitutional supercooling in the liquid ahead of the solid-liquid interface, as shown in Figure 22.

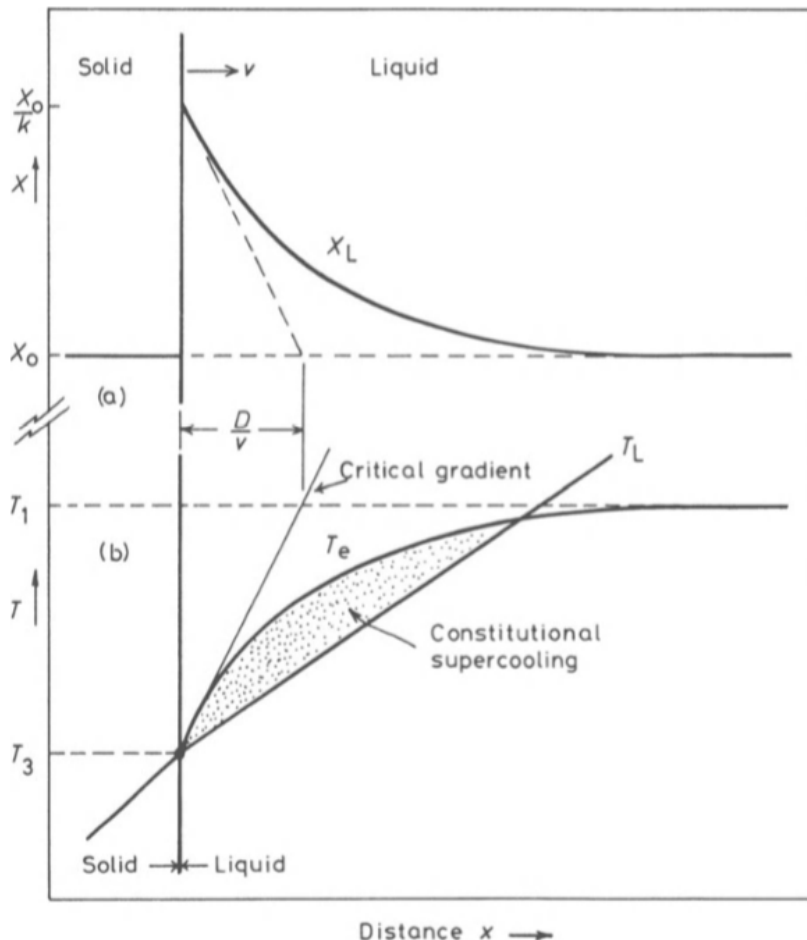


Figure 22. Schematic of constitutional supercooling [51] in the liquid ahead of the solid-liquid interface with a positive temperature gradient in the liquid.

Constitutional undercooling is the result of a solute concentration gradient in the liquid whose shape depends on the rate of rejection of the solute into the liquid due to the solute partitioning at the moving s-l

interface and the extent of diffusion that occurs in the liquid. Based on the solute concentration, it is possible to describe a solidus temperature profile in the liquid. In the presence of a steep temperature gradient in the liquid, it is possible that the actual temperature in the liquid is always higher than the local solidus. Under such conditions, the s-l interface is stable and remains as a planar front. However, if the curves representing the actual temperature and the solidus temperature intersect as shown in Figure 22, then the s-l interface becomes unstable and transitions into either cellular or cellular-dendritic mode.

In the context of additive manufacturing or rapid solidification, the ability to capture the solidification morphology whether it is cellular or cellular-dendritic depends on accurately capturing the solute partitioning, temperature, s-l interface velocity and the distribution of temperature and the solute concentration in the liquid. However, uncertainties exist in the simulations. For example, the s-l interface velocity is a product of the interface mobility and the thermodynamic driving force. Uncertainties in the interface velocity arise from the uncertainty associated with phase field mobility and its variation with temperature as well as the thermodynamic driving force because of the use of a simplified Ni-Fe-Nb ternary to represent the multi-component 718 alloy. The biggest uncertainty is in the temporal variation of temperature of the simulation volume. The initial temperature distribution is obtained by mapping the temperature data from the coarse mesh and mapping it to the finer phase field mesh. Time dependent, face-averaged thermal flux boundary conditions are obtained from the continuum code and imposed on the phase-field simulation volume. The thermal boundary conditions from the continuum code are as a result of using a set of thermophysical parameters such as thermal conductivity, specific heat and latent heat of solidification. In general, the temperature variation of these properties is not well known for a complex alloy such as 718. The latent heat in continuum codes is modeled as a constant quantity that comes out evenly between the solidus and liquidus temperatures. However, the solidus and liquidus temperatures calculated on the basis of alloy thermodynamics do not coincide with published hand-book values. Secondly, the specific heat and enthalpy as a function of temperature and local composition were calculated within the phase-field code using the Calphad model and they did not coincide with the constant values used in the continuum code. In the absence of an iterative, two-way coupling between the continuum heat transfer code and the microscopic heat transfer code, there is no consistency in the prediction of the temperature field inside the microscopic volume between the two codes. Therefore, it is almost impossible to obtain a one-to-one correspondence between simulations and experimental predictions based on the coupling approach used. However, an attempt was made to demonstrate the capability to couple the phase field simulations with thermal boundary conditions provided by UTRC, and even with the simplifications involved, one can obtain useful insights regarding the solidification microstructures under AM processing conditions.

The thermal boundary conditions shown in Table 4 were provided by UTRC for bead-on-plate welding test problem on a 718 plate using a welding power of 120W and a welding speed of 200 mm/s with a specific power of 0.6 J/mm. Columnar dendritic microstructure was obtained within the weld pool with a primary arm spacing of 577 nm and a secondary arm spacing of 240 nm. Compositional analysis of the microstructures indicated only minor segregation of Nb in the interdendritic space, although the single line scan result was not representative of the Nb segregation in the dendritic microstructure over the whole cross section. The pseudo-3D as well as full 3-D simulations results shown in Figures 10 and 12, respectively, that were carried out by using the UTRC boundary conditions, however, indicate an essentially cellular mode of solidification, although there is some indication of a cellular to dendritic transition in some locations. The primary cell width is about 3000 – 4000 nm and the indication of a secondary arm width of about 500 nm. While the experimentally measured secondary arm width of 277 nm is somewhat close to the simulation results, the primary arm spacing is almost an order of magnitude larger than experimentally observed values. The differences are attributed to the uncertainties in the model parameters described above.

## 5. SUBJECT INVENTIONS

No inventions have occurred as part of this CRADA. A journal article summarizing the work done in the CRADA will be submitted in December for publication in the Journal of Metal Minerals and Materials. The enhancements performed to MEUMAPPS and AMPE will become part of the open source code that is further being developed as part of the Exascale Computing Project (ECP) on Additive Manufacturing, ExAM which will be released in the near future.

## 6. COMMERCIALIZATION POSSIBILITIES

No commercialization possibilities exist at this time because the work was carried out on a model ternary alloy and further work is required to develop a good match between simulation and experiment on the primary arm spacing.

## 7. PLANS FOR FUTURE COLLABORATION

The HPC effort undertaken as part of this project is the first step towards the full 3-D implementation of the integrated microstructural modeling framework for AM envisioned by UTRC. The full implementation should allow tracking 3D grain morphology and provide data on texture. However, in the reduced form the ORNL approach should allow tracking the segregation correctly and by including more elements will allow prediction of deleterious phases in the as-built deposit. Potentially by including seeds within the geometry, phase field approach can predict transition phenomena in the additive manufacturing process. Furthermore, the primary and secondary dendrite arm spacing obtained from the model can be used to couple the mechanical properties with the simulated microstructure. However, several uncertainties in model parameters and alloy thermodynamics have to be addressed before the phase field simulations can be exploited for AM alloy design which is a longer term goal of UTRC. One important step in achieving this goal is proper coupling between the meso-scale CFD and micro-scale PF model. There should be a consistency between the thermo-physical properties such as thermal conductivity, specific heat and latent heat of solidification used in the continuum heat transfer model and the phase field simulations. The time and spatial resolution of the continuum heat transfer code can be improved using parallelizable CFD code such as TRUCHAS so that the accuracy of coupling with phase field simulations can be further improved.

Future effort will also involve the definition of grand challenge problems in materials processing-microstructure-property relationships applicable to additive manufacturing and will provide the basis for an INCITE proposal involving UTRC, ORNL and LLNL to enhance the impact of HPC on AM technology. The design of new alloys for AM cannot be met unless high fidelity models can be exploited. The ability to develop high fidelity, predictive models is essential for undertaking such an effort. The effort resulting from this project has positioned the team to respond to future funding opportunities in alloy design for AM technology. This will enable designing of alloy for AM processes, as well as to enhance particular properties of an alloy e.g. corrosion, oxidation etc. This has been included in recent roadmap for LIFT in collaboration with ORNL. The team can also use the HPC4materials platform to augment the phase field code so that it predicts the heat treated microstructure starting from simulated or experimental as-deposit microstructure in additive manufacturing. Phase field solution also generates 3D dendritic orientation map and it is important to correlate that with experimental data on texture obtained through electron back scattered diffraction (EBSD). Development of the post-processing tool to resolve the texture and the grain size will be important as well. This will allow completing the process microstructure map through simulation that can be directly coupled with mechanical properties that can be estimated through grain size.

## 8. CONCLUSIONS

Large scale phase field simulations of the solidification were carried out using the phase field codes at ORNL (MEUMAPPS) and LLNL (AMPE). The capabilities of both codes were enhanced to be able to run solidification problems. The focus of the effort with AMPE code was to incorporate the UTRC phase field model and demonstrate large-scale 3-D simulations in a model binary alloy. There were some issues in translating the dimensionless phase field and alloy parameters used in the UTRC model to the corresponding dimensional parameters used in AMPE. This led to the identification of the correct mesh resolution to simulate dendrites in the model alloy. Improvements were made to the original parameter set in the UTRC model to achieve the correct level of diffuseness in the solid-liquid interface. The lack of solute-partitioning using the UTRC parameters was corrected by either scaling down the kinetic coefficient or scaling up the diffusion coefficient in the model. The physical reasoning behind these changes were not fully understood. However, the ability to demonstrate multiple dendrite evolution in 3D using HPC was demonstrated. The focus of the effort with MEUMAPPS was to use the Kim-Kim-Suzuki model [43] along with dimensional phase field parameters in a model ternary Ni-Fe-Nb alloy along with integration of alloy thermodynamics to simulate dendritic solidification in the Ni-base alloy 718. The challenges associated with modeling solidification with orders of magnitude difference between the diffusion coefficient of solute in liquid and solid phases resulted in changing the solution approach from semi-implicit to an explicit finite-difference technique. Time-dependent, face-averaged, thermal boundary conditions provided by UTRC were used to drive the solidification problem. Multiple dendrite evolution using HPC and a pseudo-3D approach was demonstrated under a wide variety of boundary conditions using the explicit finite-difference code. These simulations showed that the solidification in the cellular-dendritic mode was controlled by the cooling flux in the  $z=0$  plane and also by the initial temperature distribution in the model. Full 3-D simulations of multiple dendrite evolution were carried out using the model Ni-Fe-Nb ternary alloy and the thermal boundary conditions provided by UTRC using the HPC capabilities at ORNL. Although the simulations were able to reasonably capture the width of the secondary dendrite arms seen in single track experiments using alloy 718, the simulations overestimated the width of the primary columns. Uncertainties in the simulation parameters and the thermodynamics of the alloy were responsible for the deviation. Simulations captured the partitioning of Nb to the inter-cellular and interdendritic liquid. However, the simulations overestimated the Nb segregation compared to experimental findings due to uncertainties in phase field model parameters and in the coupling of the phase field with the continuum heat transfer simulations.

## Appendix A: Ternary phase field model used in MEUMAPPS

The basic equations in the phase field model for solidification of a ternary alloy and the procedure used to solve them are described below. The evolution of the temperature field is given by

$$\frac{\partial T}{\partial t} = \nabla \cdot (\alpha_T \nabla T) + \frac{L}{C_p} \frac{\partial \phi}{\partial t}$$

In the above equation,  $\alpha_T$  is the thermal diffusivity,  $L$  is the latent heat, and  $C_p$  is the specific heat capacity. The thermal diffusivity is given by  $\alpha_T = k/\rho C_p$ , where  $k$  is the thermal conductivity and  $\rho$  is the density.

Using the approach of Kim (Acta Mater., 55, 4391-4399, 2007), the evolution equation for concentration of species  $i$  is written as

$$\frac{\partial c_i}{\partial t} = \nabla \cdot [h(\phi) D^S \nabla c_i^S + \{1 - h(\phi)\} D^L \nabla c_i^L]$$

where  $D_i^S$  and  $D_i^L$  are the diffusivities of species  $i$  in the solid and liquid, respectively, and  $h(\phi)$  is an interpolation function, taken in this work to be equal to  $\phi$ , the phase field order parameter that differentiates the solid ( $\phi = 1$ ) and liquid ( $\phi = 0$ ) phases.  $D_i(\phi)$  is the diffusivity of species  $i$ , given by

$$D_i(\phi) = h(\phi) D_i^S + [1 - h(\phi)] D_i^L$$

The interpolation function  $p(\phi)$  is given in terms of the order parameter  $\phi$  as

$$p(\phi) = \phi^3(6\phi^2 - 15\phi + 10)$$

The free energy density  $f$  is typically written in terms of the bulk free energy density of the solid and liquid phases using the interpolation function  $p(\phi)$  as

$$f = p(\phi) \overline{G^S}(c_1^S, c_2^S, T) + [1 - p(\phi)] \overline{G^L}(c_1^L, c_2^L, T) + Wg(\phi)$$

where  $c_i^S$  and  $c_i^L$  are the concentrations of species  $i$  in the solid and liquid phases. The last term in the above equation models the energy barrier associated with the interface between the solid and liquid phases, given by height  $W$ , and double-well potential  $g(\phi)$ , written as

$$g(\phi) = \phi(1 - \phi)$$

The concentration of each species is also expressed using the interpolation function  $p(\phi)$  as

$$c_i = p(\phi) c_i^S + [1 - p(\phi)] c_i^L$$

In the Kim-Kim-Suzuki (KKS) approach, it is assumed that the chemical potential for each species is the same in the solid and liquid phases, so that for each species  $i$

$$\frac{\partial G^S}{\partial c_i^S} = \frac{\partial G^L}{\partial c_i^L}$$

Next, we need to develop the evolution equation for the phase field variable  $\phi$ . Here again we follow the approach of KKS and write the equation as

$$\frac{\partial \phi}{\partial t} = M(\varepsilon^2 \nabla^2 \phi - f_\phi)$$

where  $M$  is the phase field mobility parameter and  $\varepsilon^2$  is the gradient coefficient. The derivative of the free energy density with respect to  $\phi$  is given by

$$f_\phi = \frac{\partial f}{\partial \phi} = p'(\phi) \left\{ [G^S - G^L] + \frac{\partial G^S}{\partial c_1^S} (c_1^L - c_1^S) + \frac{\partial G^S}{\partial c_2^S} (c_2^L - c_2^S) \right\} + W g'(\phi)$$

In the above equation,  $p'(\phi)$  is the derivative of  $p(\phi)$  with respect to  $\phi$ .

The inclusion of anisotropy in the interface energy leads to an expression for  $\varepsilon$  given in two-dimensions by

$$\varepsilon = \tilde{\varepsilon} \sigma(\theta) = \tilde{\varepsilon} [1 + \delta \cos\{j(\theta - \theta_0)\}]$$

where  $\tilde{\varepsilon}$  is a constant related to an energy penalty based on interface thickness,  $\delta$  represents the strength of the anisotropy,  $j$  represents the order of the crystal symmetry ( $j=4$  for cubic crystals with four-fold symmetry), and  $\theta_0$  is the initial orientation of a dendrite nucleus. The evolution equation for  $\phi$  is then given by

$$\frac{\partial \phi}{\partial t} = M \left( \tilde{\varepsilon}^2 \nabla \cdot \left\{ \begin{bmatrix} \sigma^2 & -\sigma\sigma' \\ \sigma\sigma' & \sigma^2 \end{bmatrix} \nabla \phi \right\} - f_\phi \right)$$

In the above expression,  $\sigma' = \frac{d\sigma}{d\theta} = -j\delta \sin\{j(\theta - \theta_0)\}$ . The evolution equation can be expanded as

$$\frac{\partial \phi}{\partial t} = M \tilde{\varepsilon}^2 \left( \sigma^2 \nabla^2 \phi + \nabla \sigma^2 \cdot \nabla \phi - \frac{\partial}{\partial x} \left( \sigma\sigma' \frac{\partial \phi}{\partial y} \right) + \frac{\partial}{\partial y} \left( \sigma\sigma' \frac{\partial \phi}{\partial x} \right) \right) - M f_\phi$$

The above equations have also been extended to consider anisotropy in the interface energy for a general three-dimensional system. The approach involves writing a general expression for the evolution of  $\phi$  as

$$\frac{\partial \phi}{\partial t} = M \left( \nabla \cdot \frac{\partial f_{grad}}{\partial (\nabla \phi)} - f_\phi \right)$$

where

$$f_{grad} = \frac{\sigma^2}{2} |\nabla \phi|^2$$

and

$$\sigma = \sigma(\nabla \phi) = \sigma(n'_x, n'_y, n'_z)$$

In the above expression, the components of the vector  $\mathbf{n}'$  are given by the rotation matrix that transforms the interface normal vector  $\mathbf{n}$  given in the global coordinate system to a local coordinate system that is associated with the orientation of that particular dendrite. Thus

$$\begin{aligned}
n'_x &= r_{11}n_x + r_{12}n_y + r_{13}n_z \\
n'_y &= r_{21}n_x + r_{22}n_y + r_{23}n_z \\
n'_z &= r_{31}n_x + r_{32}n_y + r_{33}n_z
\end{aligned}$$

with

$$n_x = \frac{\partial\phi/\partial x}{|\nabla\phi|}, \quad n_y = \frac{\partial\phi/\partial y}{|\nabla\phi|}, \quad n_z = \frac{\partial\phi/\partial z}{|\nabla\phi|}$$

and  $r_{ij}$  being the components of the rotation matrix.

Using the above expressions, it can be shown that the evolution equation for  $\phi$  can be written as

$$\frac{\partial\phi}{\partial t} = M \left( \nabla\sigma^2 \cdot \nabla\phi + \sigma^2 \nabla^2\phi + \nabla \cdot \left\{ |\nabla\phi|^2 \sigma \frac{\partial\sigma}{\partial(\nabla\phi)} \right\} - f_\phi \right)$$

with

$$\begin{aligned}
& \nabla \cdot \left\{ |\nabla\phi|^2 \sigma \frac{\partial\sigma}{\partial(\nabla\phi)} \right\} \\
&= \frac{\partial}{\partial x} \left[ \sigma |\nabla\phi| \left\{ \frac{\partial\sigma}{\partial n'_x} (r_{11} - n_x n'_x) + \frac{\partial\sigma}{\partial n'_y} (r_{21} - n_x n'_y) + \frac{\partial\sigma}{\partial n'_z} (r_{31} - n_x n'_z) \right\} \right] \\
&+ \frac{\partial}{\partial y} \left[ \sigma |\nabla\phi| \left\{ \frac{\partial\sigma}{\partial n'_x} (r_{12} - n_y n'_x) + \frac{\partial\sigma}{\partial n'_y} (r_{22} - n_y n'_y) + \frac{\partial\sigma}{\partial n'_z} (r_{32} - n_y n'_z) \right\} \right] \\
&+ \frac{\partial}{\partial z} \left[ \sigma |\nabla\phi| \left\{ \frac{\partial\sigma}{\partial n'_x} (r_{13} - n_z n'_x) + \frac{\partial\sigma}{\partial n'_y} (r_{23} - n_z n'_y) + \frac{\partial\sigma}{\partial n'_z} (r_{33} - n_z n'_z) \right\} \right]
\end{aligned}$$

and

$$\sigma = \tilde{\varepsilon}(1 - 3\delta) \left[ 1 + \frac{4\delta}{1 - 3\delta} \left\{ (n'_x)^4 + (n'_y)^4 + (n'_z)^4 \right\} \right]$$

In order to solve the evolution equations for  $T$ ,  $c_i$  and  $\phi$ , we make use of an explicit finite difference scheme. The evolution equation for temperature is therefore written as

$$\frac{T_{i,j}^{n+1} - T_{i,j}^n}{\Delta t} = \frac{\partial}{\partial x} \left[ \alpha_T \left( \frac{T_{i+1,j}^n - T_{i-1,j}^n}{2\Delta x} \right) \right] + \frac{\partial}{\partial y} \left[ \alpha_T \left( \frac{T_{i,j+1}^n - T_{i,j-1}^n}{2\Delta y} \right) \right] + \frac{L}{C_p} \left( \frac{\phi_{i,j}^{n+1} - \phi_{i,j}^n}{\Delta t} \right)$$

In the above expression, a forward difference scheme is used to express  $\frac{\partial T}{\partial t}$  on the left-hand side and  $\frac{\partial\phi}{\partial t}$  on the right-hand side, while a second-order accurate centered difference scheme is used to evaluate  $\nabla T$  on the right-hand side. For grid points at the domain boundaries, the centered difference approximations were replaced by forward or backward difference approximations as appropriate. A similar approach is used to solve for the concentration of each species and the phase field variable, based on the evolution equations for  $c_i$  and  $\phi$ .

The terms involving the bulk free energy in each phase and their gradients were calculated based on expressions for  $G^S$  and  $G^L$  taken from thermodynamic database. At each time step, based on the current values of  $T$ ,  $c_i$  and  $\phi$ , the corresponding values of  $c_i^S$  and  $c_i^L$  were computed. The values of the specific heat  $C_p$  and the latent heat  $L$  were also obtained during this calculation based on the local change in enthalpy.

## BIBLIOGRAPHY

1. E. Herderick, Additive Manufacturing of Metals: A Review, Proceedings of MS&T11, Additive Manufacturing of Metals, Columbus, OH, 2011
2. Zhang, Tong, Zheng, Zhentai, and Zhao, Rui, "A Dynamic Welding Heat Source Model in Pulsed Current Gas Tungsten Arc Welding," *Journal of Materials Processing Technology*, Vol. 213, No. 12, 2013, pp. 2329–2338.
3. Shen, Ninggang (George) and Chou, Kevin, "Thermal Modeling of Electron Beam Additive Manufacturing Process— Powder Sintering Effects," Proc. the 7th ASME 2012 International Manufacturing Science and Engineering Conference (MSEC2012), 2012, ASME.
4. Peng, Y., Wang, K. H., Zhou, Q., Wang, Y. J., and Fu, P. F., "Beam Quality Test Technology and Devices of Electron Beam Welding," *Vacuum*, Vol. 86, No. 3, 2011, pp. 261–266.
5. Elmer, J. W. and Teruya, A. T., "An Enhanced Faraday Cup for Rapid Determination of Power Density Distribution in Electron Beams," *Welding Journal*, Vol. 80, No. 12, 2001, pp. 288S–295S.
6. Palmer, T. A. and Elmer, J. W., "Characterization of Electron Beams at Different Focus Settings and Work Distances in Multiple Welders Using the Enhanced Modified Faraday Cup," *Science and Technology of Welding and Joining*, Vol. 12, No. 2, 2007, pp. 161–174.
7. Palmer, T.A., Elmer, J. W., Nicklas, K. D. and Mustaleski, T., "Transferring Electron Beam Welding Parameters Using the Enhanced Modified Faraday Cup," *Welding Journal*, Vol. 86, No. 12, 2007, p. 388S–398S.
8. Palmer, T. A. and Elmer, J. W. "Improving Process Control in Electron Beam Welding Using the Enhanced Modified Faraday Cup," *Journal of Manufacturing Science and Engineering-Transactions of the ASME*, Vol. 130, No. 4, 10 July 2008.
9. Safdar, S., Li, L., and Sheikh, M. A., "Numerical Analysis of the Effects of Nonconventional Laser Beam Geometries during Laser Melting of Metallic Materials," *Journal of Physics D-Applied Physics*, Vol. 40, No. 2, 2007, pp. 593–603.
10. Nath, A. K., Sridhar, R., Ganesh, P., and Kaul, R., "Laser Power Coupling Efficiency in Conduction and Keyhole Welding of Austenitic Stainless Steel," *Sadhana-Academy Proceedings in Engineering Sciences*, Vol. 27, Part 3, June 2002, pp. 383–392.
11. Amanda S. Wu · Donald W. Brown · Mukul Kumar · Gilbert F. Gallegos · Wayne E. King, 2014, 'An Experimental Investigation into Additive Manufacturing-Induced Residual Stresses in 316L Stainless Steel', *Metallurgical and Materials Transactions A* 12/2014; 45(13).
12. Wei, P. S., Lin, C. L., Liu, H. J., and Ting, C. N., "Transient Thermocapillary Convection in a Molten or Weld Pool," *Journal of Manufacturing Science and Engineering-Transactions of the ASME*, Vol. 134, No. 1, 11 January 2012.
13. Wei, P. S. and Liu, H. J., "Scaling Thermocapillary Weld Pool Shape and Transport Variables in Metals," *Welding Journal*, Vol. 91, No. 7, 2012, pp. 187S–194S.
14. Fan, Zhiqiang and Liou, Frank, "Numerical Modeling of the Additive Manufacturing (AM) Processes of Titanium Alloy, in Titanium Alloys," *Towards Achieving Enhanced Properties for Diversified Applications*, ed. A. K. M. Nurul Amin, Rijeka, Croatia, In Tech, 2012, pp. 3–28.
15. Daneshkhah, R., Najafi, M., and Torabian, H., "Numerical Simulation of Weld Pool Shape during Laser Beam Welding," *International Research Journal of Applied and Basic Sciences*, Vol. 3, No. 8, 2012, pp. 1624–1630.
16. Zhang, W., Liu, Y., Wang, X., and Zhang, Y. M., "Characterization of Three-dimensional Weld Pool Surface in GTAW," *Welding Journal*, Vol. 91, No. 7, July 2012, pp. 195S–203S.
17. Manvatkar, V. D., Gokhale, A. A., Reddy, G. Jagan, Venkataramana, A., and De, A., "Estimation of Melt Pool Dimensions, Thermal Cycle, and Hardness Distribution in the Laser-engineered Net Shaping Process of Austenitic Stainless Steel," *Metallurgical and Materials Transactions A—Physical Metallurgy and Materials Science*, Vol. 42, No. 13, December 2011, pp. 4080–4087.
18. Rai, R., Palmer, T. A., Elmer, J. W., and DebRoy, T., "Heat Transfer and Fluid Flow during Electron Beam

- Welding of 304L Stainless Steel Alloy," *Welding Journal*, Vol. 88, No. 3, March 2009, pp. 54S–61S.
19. Rai, R., Burgardt, P., Milewski, J. O., Lienert, T. J., and DebRoy, T., "Heat Transfer and Fluid Flow during Electron Beam Welding of 21Cr–6Ni–9Mn Steel and Ti–6Al–4V Alloy," *Journal of Physics D—Applied Physics*, Vol. 42, No. 2, 2009.
  20. Rai, R., Kelly, S. M., Martukanitz, R. P., and DebRoy, T., "A Convective Heat-transfer Model for Partial and Full Penetration Keyhole Mode Laser Welding of a Structural Steel," *Metallurgical and Materials Transactions A—Physical Metallurgy and Materials Science*, Vol. 39A, No. 1, January 2008, pp. 98–112.
  21. Vasinonta, A., Beuth, J. L., and Griffith, M., "Process Maps for Predicting Residual Stress and Melt Pool Size in the Laser-based Fabrication of Thin-walled Structures," *Journal of Manufacturing Science and Engineering—Transactions of the Asme*, Vol. 129, No. 1, 2007, pp. 101–109.
  22. Vasinonta, A., Beuth, J., and Griffith, M., "Process Maps for Controlling Residual Stress and Melt Pool Size in Laser-based SFF Processes," *Proc. Solid Freeform Fabrication Symposium*, Austin, 2000.
  23. Lindgren, Lars-Erik, Lundbäck, Andreas, and Fisk, M., "Thermo-Mechanics and Microstructure Evolution in Manufacturing Simulations," *Journal of Thermal Stresses*, Vol. 36, No. 6, 2013, pp. 564–588.
  24. Ding, J., Colegrove, P., Mehnen, J., Ganguly, S., Almeida, P. M. Sequeira, Wang, F., Williams, S., "Thermo-mechanical Analysis of Wire and Arc Additive Layer Manufacturing Process on Large Multi-layer Parts," *Computational Materials Science*, Vol. 50, No. 12, December 2011, pp. 3315–3322.
  25. Wayne E. King · Holly D. Barth · Victor M. Castillo · Gilbert F. Gallegos · John W. Gibbs · Douglas E. Hahn · Chandrika Kamath · Alexander M. Rubenchik, "Observation of keyhole-mode laser melting in laser powder-bed fusion additive manufacturing", *Journal of Materials Processing Technology* 12/2014; 214(12):2915–2925.
  26. Zhang, Jingwei, Liou, Frank, Seufzer, William, Newkirk, Joseph, Fab, Zhiqiang, Liu, Heng, Sparks, Todd E., "Probabilistic Simulation of Solidification Microstructure Evolution during Laser-based Metal Deposition," 24th Annual International Solid Freeform Fabrication Symposium, Austin, 2013.
  27. Eshraghi, Mohsen, Felicelli, Sergio D., and Jelinek, Bohumir, "Three Dimensional Simulation of Solutal Dendrite Growth Using Lattice Boltzmann and Cellular Automaton Methods," *Journal of Crystal Growth*, Vol. 354, No. 1, 1 September 2012, pp. 129–134.
  28. Eshraghi, M. and Felicelli, S. D., "An Implicit Lattice Boltzmann Model for Heat Conduction with Phase Change," *International Journal of Heat and Mass Transfer*, Vol. 55, No. 9–10, 2012, pp. 2420–2428.
  29. Barrales-Mora, L. A., Gottstein, G., and Shvindlerman, L. S., "Effect of a Finite Boundary Junction Mobility on the Growth Rate of Grains in Two-dimensional Polycrystals," *Acta Materialia*, Vol. 60, No. 2, 2012, pp. 546–555.
  30. Amooezaei, M., Gurevich, S., and Provatas, N., "Orientation Selection in Solidification Patterning," *Acta Materialia*, Vol. 60, No. 2, 2012, pp. 657–663.
  31. Brandl, Erhard, Michailov, Vesselin, Viehweger, Bernd, and Leyens, Christoph, "Deposition of Ti–6Al–4V Using Laser and Wire, Part I: Microstructural Properties of Single Beads," *Surface & Coatings Technology*, Vol. 206, No. 6, 15 December 2011, pp. 1120–1129.
  32. Groeber, M. A., "Digital Representation of Materials Grain Structure," *Computational Methods for Microstructure-Property Relationships*, ed. Somnath Ghosh and Dennis Dimiduk, United States: Springer, 2010, pp. 53–97.
  33. Barrales-Mora, L. A., Gottstein, G., and Shvindlerman, L. S., "Three-dimensional Grain Growth: Analytical Approaches and Computer Simulations," *Acta Materialia*, Vol. 56, No. 20, 2008, pp. 5915–5926.
  34. Bontha, Srikanth, Klingbeil, Nathan W., Kobryn, Pamela A., and Fraser, Hamish L., "Thermal Process Maps for Predicting Solidification Microstructure in Laser Fabrication of Thin-wall Structures," *Journal of Materials Processing Technology*, Vol. 178, No. 1–3, 2006, pp. 135–142.
  35. Demirel, M. C., Kuprat, A. P., George, D. C. and Rollett, A. D., "Bridging Simulations and Experiments in Microstructure Evolution," *Physical Review Letters*, Vol. 90, No. 1, 9 January 2003.
  36. Yang, Z., Sista, S., Elmer, J. W., and DebRoy, T., "Three-dimensional Monte Carlo Simulation of Grain Growth during GTA Welding of Titanium," *Acta Materialia*, Vol. 48, No. 20, 4 December 2000, pp. 4813–4825.
  37. Wayne King LLNL 2016 TMS Annual Meeting & Exhibition
  38. Alonso Peralta Honeywell Additive manufacturing scalability, implementation, readiness, and transition

39. Acharya R, Sharon J, Staroselsky A, Prediction of Microstructure in Laser Powder Bed Fusion Process,” *Acta Materialia*, vol. 124, 2017, pp. 360-371.
40. Shibuta Y, Ohno M, Takaki T, “Solidification in a supercomputer: From crystal nuclei to dendrite assemblages”, *JOM*, Vol 67 (8), 2015, pp1793-1804.
41. Kobayashi, R., “Modeling and Numerical Simulations of Dendritic Crystal Growth,” *Physica D*, Vol. 63, 1993, pp. 410-423.
42. Aziz, M.J. and Kaplan, T., “Continuous Growth Model for Interface Motion during Alloy Solidification,” *Acta Metall.*, 36, 1988, pp. 2335-2347.
43. S.G. Kim, W.T. Kim and T. Suzuki, *Phys Rev E*, 1999, vol. 60, pp. 7186-7197
44. Chen, L.Q., and Shen, J., “Applications of Semi-Implicit Fourier-Spectral Method to Phase Field Equations,” *Computer Phys. Comm.*, 108, 1998, pp. 147-158.
45. M. R. Dorr, J.-L. Fattebert, M. E. Wickett, J. F. Belak, P. E. A. Turchi, “A Numerical Algorithm for the Solution of a Phase-Field Model of Polycrystalline materials”, *J. Comp. Phys.* 229 (3), p. 626-641 (2010)
46. Fattebert, J.-L.; Wickett, M. E.; Turchi, P. E. A, “Phase-field modeling of coring during solidification of Au- Ni alloy using quaternions and CALPHAD input”, *ACTA MATERIALIA*, 62, (2014), 89-104.
47. Takaki, T., “Phase-field Modeling and Simulations of Dendrite Growth,” *ISIJ International.*, 54, 2014, pp. 437-444.
48. Karma, A., and Rappel, W.-J., “Quantitative Phase-Field Modeling of Dendrite Growth in Two and Three Dimensions,” *Phy. Rev. E*, 57, 1998, 4323-4349.
49. Boettinger, W.A., Warren, J.A., Beckermann, C and Karma, A., “Phase Field Simulation of Solidification,” *Annual Review of Materials Research*, Vol. 32, 2002, pp. 163-194.
50. Beckermann, C., Diepers, H.J., Steinbach, I., Karma, A., and Tong, X., “Modeling melt convection in phase-field simulations of solidification”, *Journal of Computational Physics*, Vol. 154, 1999, pp. 468-496.
51. Porter, D.A. and Easterling, K.E., “Phase Transformations in Metals and Alloys,” Springer Science + Business Media, B.V., Hong Kong, 1992.